10. SITE 934[1]

Shipboard Scientific Party[2]

HOLE 934A

Date occupied: 15 April 1994

Date departed: 16 April 1994

Time on hole: 19 hr

Position: 5°29.047′N, 47°40.857′W

Bottom felt (drill pipe measurement from rig floor, m): 3432.7

Distance between rig floor and sea level (m): 10.96

Water depth (drill pipe measurement from sea level, m): 3421.7

Penetration (m): 108.80

Number of cores (including cores having no recovery): 12

Total length of cored section (m): 108.80

Total core recovered (m): 111.65

Core recovery (%): 102

Oldest sediment cored:
Depth (mbsf): 108.80
Nature: Silty clay
Earliest age: Pleistocene

HOLE 934B

Date occupied: 16 April 1994

Date departed: 17 April 1994

Time on hole: 1 day, 1 hr

Position: 5°29.020′N, 47°40.860′W

Bottom felt (drill pipe measurement from rig floor, m): 3432.0

Distance between rig floor and sea level (m): 10.99

Water depth (drill pipe measurement from sea level, m): 3421.0

Penetration (m): 108.80

Number of cores (including cores having no recovery): 12

Total length of cored section (m): 108.80

Total core recovered (m): 105.92

Core recovery (%): 97

Oldest sediment cored:
Depth (mbsf): 108.80
Nature: Silty clay
Earliest age: Pleistocene

Principal results: Site 934 (proposed Site AF-15) is located in a cutoff meander bend of the main (Amazon) channel of the Amazon Fan. The site was selected from SeaBeam bathymetric and 3.5-kHz data. A short presite 3.5-kHz survey was made to verify site location. The present seafloor in the abandoned bend is 55 m shallower than the main channel floor. This elevation difference results from mud sedimentation in the abandoned meander bend and probably from incision of the main channel after the cutoff. The 100-m-deep holes allowed sampling of old channel sediment unaffected by any latest Pleistocene channel incision. A short string consisting of the resistivity and gamma tools was used to log the hole.

Hole 934A was cored by APC to 108.8 mbsf and recovered 111.66 m (102.6%). Hole 934B was offset 50 m to the south, closer to the old channel axis, and cored to 108.8 mbsf, recovering 106.92 m (98.3%). This is excellent recovery for a site with 30% sand beds. Temperature measurements were made at 63 and 82 mbsf using ADARA and show a geothermal gradient of 35°/km. Gas expansion in many cores destroyed bedding structures of most sand. Methane was found throughout the hole, but higher molecular-weight hydrocarbons were not detected. Logging of Hole 934B was hindered by initial hole collapse, but resistivity and gamma data were obtained from 50 to 103 mbsf after the hole was cleaned.

Five lithologic units are recognized:

Unit I (0–0.87 mbsf) is a Holocene, intensely bioturbated foraminifer-nannofossil clay, with up to 45% carbonate. A dark brown crust occurs at 0.48 mbsf.

Unit II (0.87–42.30 mbsf) consists of mud with thin beds and laminae of silt and sand. The unit is interpreted as sediment that filled the abandoned meander bend by spillover from turbidity currents flowing down the main Amazon Channel after the meander was cut off. Subunit IIA (0.87–7.70 mbsf) consists of prominently color-banded clays, some of which are mud turbidites with hemipelagic tops containing nannofossils. Subunit IIB (7.70–37.89 mbsf) consists of silty clays with silt laminae and some graded beds of silty sand, a few of which are more than 1 m thick. Subunit IIC (37.89–42.30 mbsf) consists of mud that is slightly color-banded and mottled. Samples from the Unit II contain 5%–20% carbonate, although generally foraminifer and nannofossil abundances are very low.

Unit III (42.30–64.56 mbsf) consists of mud with thin beds and laminae of silt and sand, which have all been affected by wet-sediment deformation, including plastic folding, injection of sand and mud, and partial mixing of different sediment types. The unit is interpreted as a slump deposit formed by sediment failure of the adjacent channel wall. This unit has distinctly higher wet-bulk density and shear strength compared with Unit II; shear strength within the unit decreases downhole.

Unit IV (64.56–97.30 mbsf) consists of medium to very thick beds of fine- to medium-grained sand and coarse silt, with thin interbeds of mud. Many of the sand beds contain mud clasts. At the top of the unit is an 18-m-thick sand bed that contains folded mud clasts up to 70 cm thick. No evidence was seen that this bed is amalgamated, but internal structures are obscured by gas expansion. Near the base of the bed are patches of 1–2 mm quartzose sand, some granules, and shell debris. This unit is interpreted as the original channel-fill sediment deposited before meander abandonment. Beds thicken from Hole 934A to 934B, which is 50 m to the south and closer to the original channel axis. Mud clasts show shear strengths of 50–120 kPa, compared with 25–50 kPa in Unit III.

Unit V (97.30–108.8 mbsf) consists of mud with thin beds and laminae of silt and sand. The mud contains a few planktonic and upper bathyal benthic foraminifers. Shear strength is similar to that of the mud clasts in Unit IV, whereas wet-bulk density is a little higher (2.0 g/cm^3, cf. 1.9 g/cm^3 in the mud clasts). The unit is interpreted as levee sediment predating the channel in the meander loop.

Foraminifer abundances are generally very low except in Unit I. A detailed abundance profile in Unit I showed that *G. fibriata* disappeared at

[1]Flood, R.D., Piper, D.J.W., Klaus, A., et al., 1995. *Proc. ODP, Init. Repts.*, 155: College Station, TX (Ocean Drilling Program).

[2]Shipboard Scientific Party is as given in the list of participants in the contents.

0.3 mbsf, *G. menardii* at 0.4 mbsf, and *G. tumida* at 0.9 mbsf. The *G. tumida* datum is taken as approximately 9 ka.

Total organic-carbon concentrations in mud range from 0.8% to 1.1%. Total sulfur is as much as 0.16% in the upper part of the sediment column, but below 29 mbsf no sulfur was detected.

The fine sand beds in Units II and IV consist of quartz (30%–50%), feldspar (5%–20%, mostly plagioclase), and mica (4%–40%). Accessory minerals include zircon, hornblende, augite, and opaque oxide minerals. Medium to coarse sand grains are texturally distinct, comprising 90% well-rounded quartz grains with iron-rich surface coatings.

We interpret the sediment at this site to represent pre-channel silt and mud (Unit V), channel-fill sand (Unit IV) and muddy slump (Unit III), overlain by overbank sedimentation into the abandoned meander loop (Unit II), and capped by the ubiquitous Holocene hemipelagic calcareous clay (Unit I). The 18-m-thick sand bed at the top of Unit IV was deposited by an unusually large flow or set of flows, probably a cohesionless debris flow, capable of transporting granules of quartz and meter-size boulders of mud. This flow deposit and the overlying contorted slump deposit may have plugged the channel, causing diversion of turbidity currents across the narrow meander neck to the west, consequently cutting off this meander loop.

SETTING AND OBJECTIVES

Introduction

Site 934 (proposed Site AF-15) is located in a cutoff meander bend of the main (Amazon) channel of the Amazon Fan. The present-day seafloor surface in the cutoff meander lies 55 m above the main channel floor. This site provided a unique opportunity to sample sediment deposited in a channel while minimizing the potential for tapping into an unsealed reservoir sand. Limited logging was undertaken to further characterize this sediment.

Setting

Site 934 is located in the central part of the Amazon Fan in a cutoff meander off the eastern (right) flank of the Amazon Channel

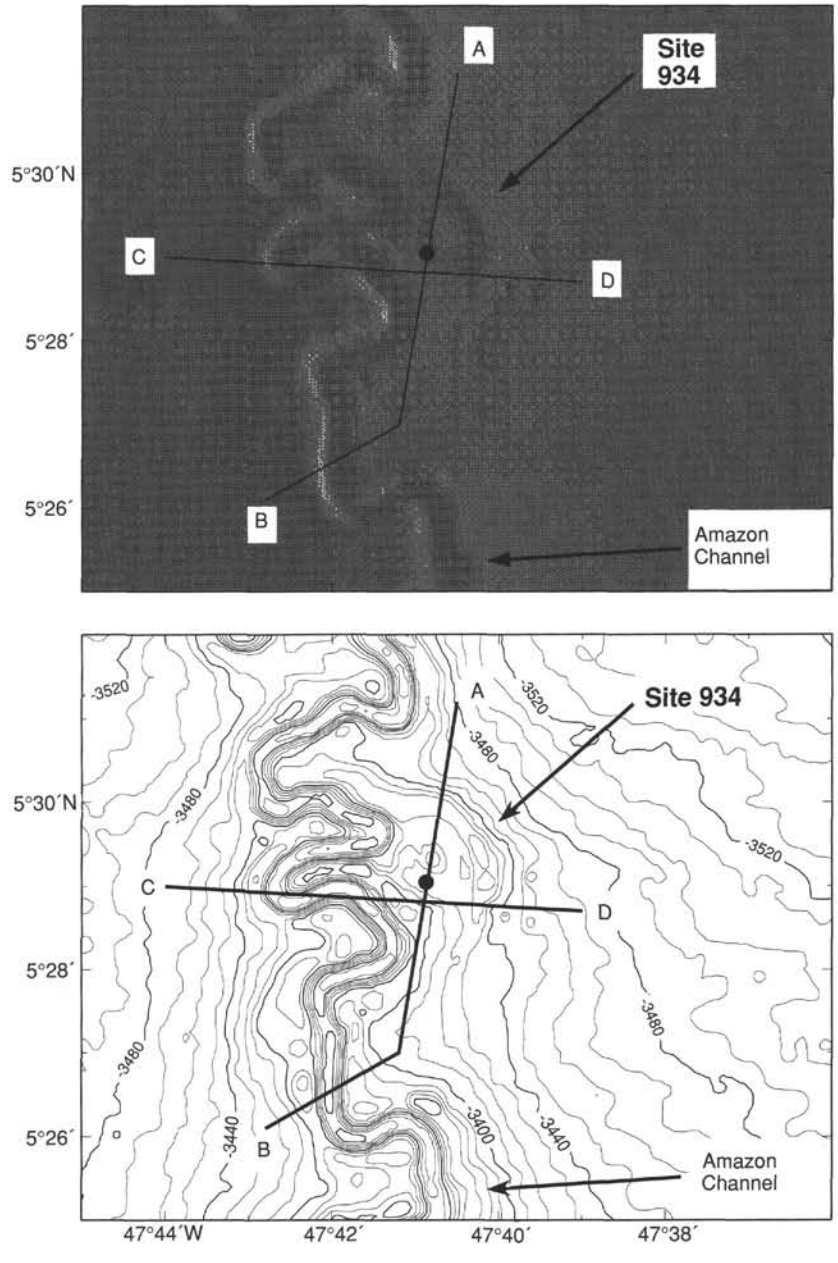

Figure 1. Detailed bathymetric map and shadowgram of Site 934 with 3.5-kHz lines (A–B and C–D).

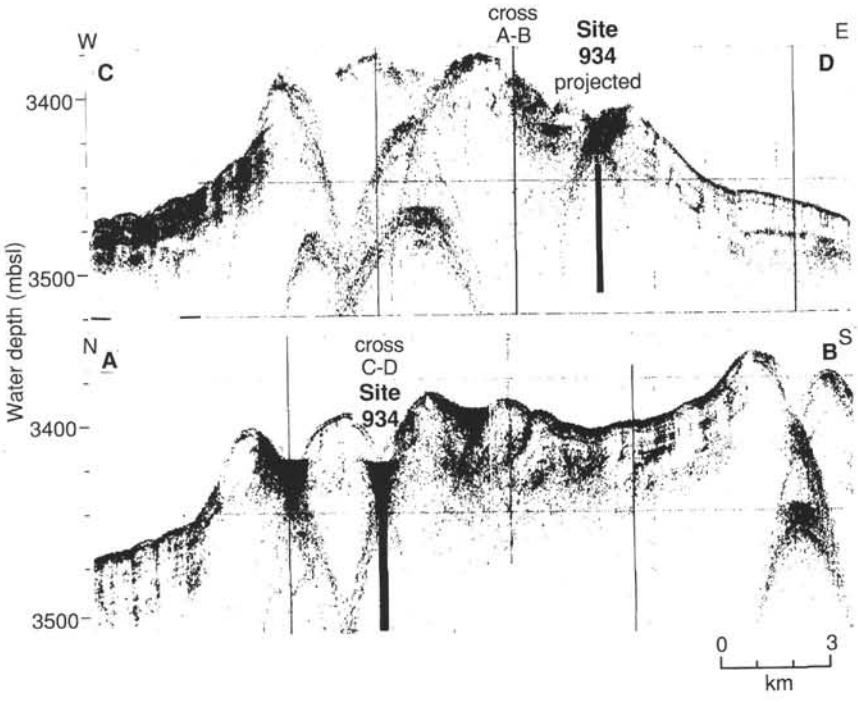

Figure 2. Two 3.5-kHz profiles through Site 934. Profiles are located on Figure 1.

(Figs. 1 and 2). The Amazon Channel in this region is 70 m deep with a sinuosity of 2.1 and an along-channel gradient of 3.5 m/km (Pirmez, 1994). When the path of the Amazon Channel included the meander, sinuosity of this section was 2.7. The present-day floor of the cutoff meander has a depth of about 20 m and a width of 350 m, and it is 55 m above the floor of the adjacent channel. Pirmez (1994) suggested that the meander cutoff was formed at the time of the avulsion of the Amazon Channel from the Brown Channel farther downstream. Avulsion is thought to cause upstream channel downcutting, and resulted in the cutting off of the meander loop. The entrenchment preserved a channel-floor deposit in the meander loop above the floor of the adjacent channel. We anticipated that the sediment would include coarse sand and contain macroscopic organic detritus.

Site 934 was selected from GLORIA side-scan sonar profiles and SeaBeam multibeam bathymetry (Fig. 2). The location was confirmed prior to drilling during a 3.5-kHz survey. Seismic profiles in the vicinity of the channel are difficult to interpret because side-echoes from the meandering channel are superimposed on reflections from beneath the channel. The high-amplitude reflections (HARs) commonly observed beneath the channel on seismic profiles (e.g., Fig. 2) are thought to be caused by this type of side-echo (Flood, 1987). The upper sediment layers at the site are thus only characterized by 3.5-kHz profiles (Fig. 2). The strong reflections from the channel floor allow little acoustic penetration at the site, and side-echoes from the channel walls mask the channel floor beneath the onlapping fill.

Objectives

The principal objectives of coring at Site 934 were:

1. Sampling and characterization of channel-floor sediment during times when the channel was an active meander and after it was cut off.
2. Estimating the time at which the cutoff occurred by dating materials that accumulated in the channel.
3. Characterizing land climate through the analysis of the coarse organic matter that accumulated in this setting.

The principal objectives of logging were to characterize the channel-floor and channel-fill sand and to allow sediment in regions of poor recovery to be characterized. Because of the shallow depth of the hole (100 m) and its potential instability, we chose to run only a short logging string with the resistivity and natural gamma tools.

OPERATIONS

Transit: Site 933 to Site 934 (AF-15)

During the transit from Site 933 to Site 934, we performed a short (~9 nmi) seismic survey over Site 935 (AF-14). We did this so that, after finishing Site 934, we could move in dynamic positioning mode to Site 935 (AF-14) without retrieving the drill string. Once we arrived near Site 934, we performed a 20-nmi, 3.5-kHz PDR survey over Site 934 to verify its position. The transit and surveys covered about 70 nmi in about 9.0 hr. We deployed a commandable retrievable beacon at 2321 hr 15 April.

Hole 934A

We assembled a bottom-hole assembly (BHA) similar to that used at Sites 930–933, but left out the 7-in. drill collar to improve the bending strength in this shallow hole, and ran the bit to the seafloor. The distance from sea level to rig floor, which depends on the ship's draft, was 10.96 m for Holes 934A and 934B. We positioned the bit at 3427.5 mbrf and spudded Hole 934A at 0625 hr 16 April. Core 1H recovered 4.29 m (Table 1), and the mud line was defined to be at 3432.7 mbrf. Cores 1H through 12H were taken from 0 to 108.8 mbsf (3432.7–3541.5 mbrf) and recovered 111.65 m of sediment (102.6%). Many of the cores recovered at Site 934 began to extrude sediment from the core liner due to gas expansion once the liner was taken out of the core barrel. Core disturbance was minimized by drilling small holes in nearly all of the core liners to allow gas to escape. The core liner of Core 7H was split while coring. The top part of the first section of Cores 5H, 6H, and 8H extruded onto the rig floor. Cores 3H through 12H were oriented with the Tensor tool, and ADARA heat-flow measurements were taken during Cores 4H and 8H. The deviation of the borehole from vertical (using the Tensor tool) was 3.3° at 23.3 mbsf, 3.3° at 32.8 mbsf, 3.8° at 42.3 mbsf, and 3.8° at 51.8 mbsf. After Core 12H we pulled the bit above the seafloor.

Table 1. Site 934 coring summary.

Core	Date (1994)	Time (UTC)	Depth (mbsf)	Length cored (m)	Length recovered (m)	Recovery (%)
155-934A-						
1H	April 16	1050	0.0–4.3	4.3	4.29	99.7
2H	April 16	1140	4.3–13.8	9.5	10.13	106.6
3H	April 16	1235	13.8–23.3	9.5	10.18	107.1
4H	April 16	1355	23.3–32.8	9.5	10.33	108.7
5H	April 16	1455	32.8–42.3	9.5	10.22	107.6
6H	April 16	1545	42.3–51.8	9.5	10.09	106.2
7H	April 16	1635	51.8–61.3	9.5	10.20	107.3
8H	April 16	1740	61.3–70.8	9.5	10.53	110.8
9H	April 16	1835	70.8–80.3	9.5	5.76	60.6
10H	April 16	1920	80.3–89.8	9.5	9.96	105.0
11H	April 16	2025	89.8–99.3	9.5	10.28	108.2
12H	April 16	2125	99.3–108.8	9.5	9.68	102.0
155-934B-						
1H	April 16	2300	0.0–7.5	7.5	7.49	99.8
2H	April 16	2350	7.5–17.5	10.0	9.25	92.5
3H	April 17	0035	17.5–26.5	9.0	10.13	112.5
4H	April 17	0135	26.5–36.0	9.5	9.51	100.0
5H	April 17	0225	36.0–45.5	9.5	10.17	107.0
6H	April 17	0310	45.5–55.0	9.5	10.82	113.9
7H	April 17	0410	55.0–64.5	9.5	10.02	105.5
8H	April 17	0510	64.5–74.0	9.5	9.75	102.0
9H	April 17	0615	74.0–83.5	9.5	9.27	97.6
10H	April 17	0720	83.5–93.0	9.5	9.25	97.3
11H	April 17	0815	93.0–102.5	9.5	4.34	45.7
12H	April 17	0915	102.5–108.8	6.3	6.92	110.0
Coring totals				108.8	106.9	98.30

Note: An expanded version of this coring summary table that includes lengths and depths of sections, location of whole-round samples, and comments on sampling disturbance is included on the CD-ROM in the back pocket of this volume.

Hole 934B

We offset the ship 50 m to the south and positioned the bit at 3430.0 mbrf. Hole 934B was spudded at 1845 hr 16 April. Core 1H recovered 7.49 m, and the mud line was defined to be at 3432.0 mbrf. Cores 1H through 12H were taken from 0 to 108.8 mbsf (3432.0–3540.8 mbrf) and recovered 106.92 m of sediment (98.3%). Cores 3H through 12H were oriented using the Tensor tool. Poorly consolidated, coarse-grained sediment was recovered from parts of the hole. The core liner of Core 6H was split during coring. The top parts of the first sections of Cores 8H and 9H extruded onto the rig floor. Cores 9H through 12H were partial strokes.

In preparation for logging, we circulated a 30-barrel mixture of sepiolite and seawater in the hole. The bit was positioned at 78 mbsf and configured so that it could be picked up 30 mbsf to log the upper part of the hole. The Dual Induction/Gamma Ray tool (DIL/GR) was only able to pass 5 m below the bit, to 83 mbsf. We picked the pipe up to 68 mbsf, but the tool still could not get past 83 mbsf. We then picked the pipe up to 58 mbsf, and this time the tool could not pass 73 mbsf. This suggested that the hole was filling in rapidly. The logging tool was pulled out, the sand bridge drilled out, and the hole was cleaned out again to 108.8 mbsf. Another 30-barrel sepiolite/seawater mixture was circulated, and the pipe was positioned at 78 mbsf. The DIL/GR was run in and found bottom at 3538 mbrf (3 m fill), and the hole was logged up to the bit at 48 mbsf.

The bit cleared the seafloor at 1750 hr 17 April and was pulled up another 100 m to prepare for the dynamic positioning transit to AF-14 (Site 935). The beacon was retrieved at 1915 hr 17 April.

LITHOSTRATIGRAPHY

Introduction

Both Holes 934A and 934B penetrated to 108.8 mbsf in an abandoned meander loop and recovered uppermost Quaternary sediment. Expansion of methane gas during core recovery commonly disrupted the primary sedimentary structures in many silt and sand beds and produced void spaces within many of the cores (see "Lithostratigraphy" section in the "Explanatory Notes" chapter, this volume). The composite lithologic section (Fig. 3) and sub-bottom depths for unit boundaries are derived from Hole 934A. Data from Hole 934B are used only below about 75 mbsf, where there are lithologic contrasts between sediment types recovered from the two holes (Fig. 4). Core 934B-12H was highly disturbed by coring, and it is unclear how much of the retrieved material actually comes from the cored interval 102.5 to 108.8 mbsf. Therefore, lithologic information from this core

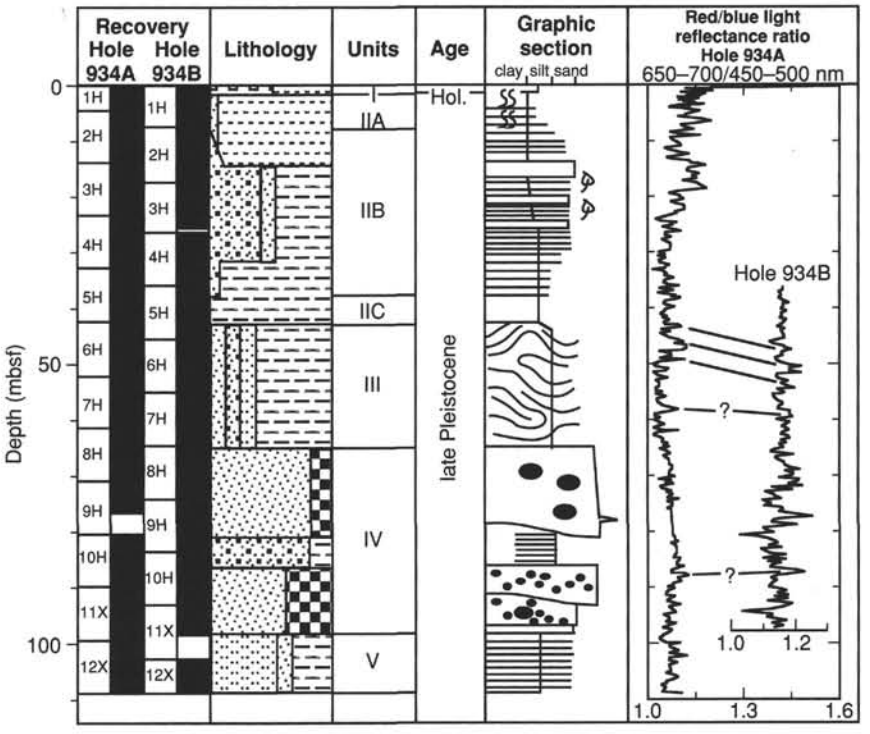

Figure 3. Composite stratigraphic section for Site 934 showing core recovery for both holes, a simplified summary of lithology for Hole 934B, depths of unit boundaries, age, a graphic section with generalized grain-size and bedding characteristics, and downhole variations in light-reflectance values. The lithologic symbols are explained in Figure 1 of the "Explanatory Notes" chapter, this volume. The light-reflectance scale for data below Subunit IIB, Hole 934B, is offset from the scale for Hole 934A; tie-lines between the two spectral profiles provide possible correlations between the two holes.

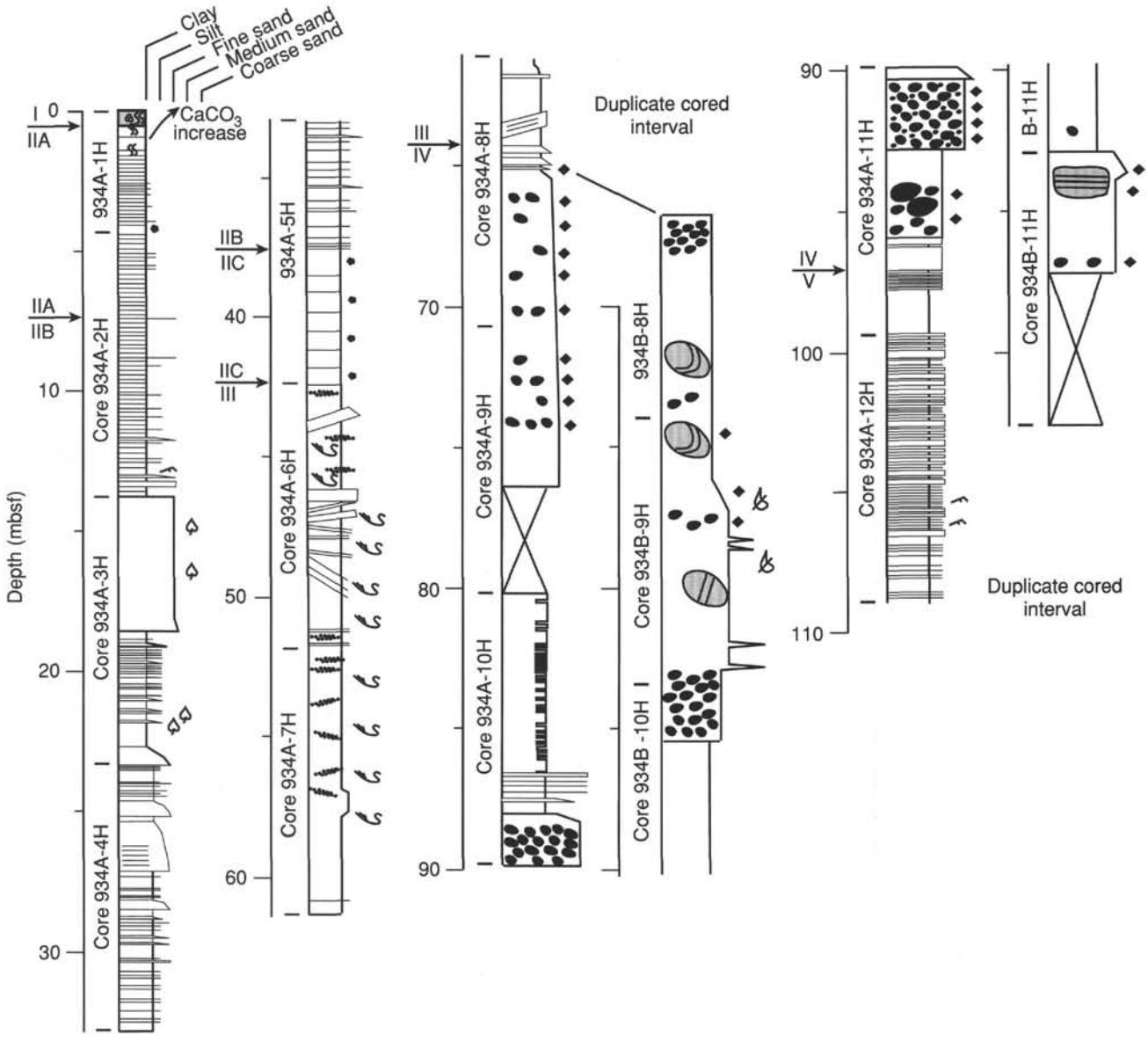

Figure 4. Graphic sedimentological columns for Site 934 showing grain-size variation (width of columns), bed thickness, and sedimentary structures; symbols and preparation of these columns are explained in the "Lithostratigraphy" section of the "Explanatory Notes" chapter, this volume. Arrows indicate the position of the boundaries of units and subunits. The upper part of the column is shown in the longitudinal profile of the foldout (back pocket, this volume) to show down-fan changes in channel-fill and related mass-failure deposits. Holes 934A and 934B cored somewhat different deposits below about 70 mbsf; parallel columns are presented to show these contrasting successions.

is not used. Five lithostratigraphic units are distinguished on the basis of mineralogy, texture, scale of interbedding, and presence of soft-sediment deformation.

Description of Lithostratigraphic Units

Unit I

Intervals: 155-934A-1H-1, 0–87 cm; 155-934B-1H-1, 0–93 cm
Age: Holocene
Depth: 0.00–0.87 mbsf

The upper part of Unit I consists of a brown (10YR 5/3) to olive brown (2.5Y 4/4) foraminifer-nannofossil clay from 0.00 to 0.47 mbsf, overlying a distinctive dark brown (10YR 3/3) iron-rich crust in the interval 934A-1H-1, 47–48 cm (0.47–0.48 mbsf). Similar iron-rich crusts were analyzed previously and correlated throughout the Amazon Fan and adjacent Guiana Basin (Damuth, 1977; see "Introduction" chapter, this volume). The crust is underlain by dark gray (5Y 4/1) nannofossil-rich clay (0.48–0.63 mbsf) and dusky greenish gray (5GY 5/1) foraminifer-nannofossil clay (0.63–0.86 mbsf), which contains rare pteropods. The base of Unit I is marked by a dark brown (7.5YR 3/2) diagenetic color band (interval 934A-1H-1, 86–87 cm). Carbonate content is about 45% in the calcareous clays (see "Organic Geochemistry" section, this chapter). The sediment of Unit I is intensely burrowed throughout.

Unit II

Intervals: 155-934A-1H-1, 87 cm, through -5H-CC, 34 cm; 155-934B-1H, 93 cm, through -5H-6 (base not recognized because of extensive coring disturbance)
Age: Holocene to late Pleistocene
Depth: 0.87–42.30 mbsf

Unit II consists predominantly of terrigenous clay and silty clay of dark olive gray (5Y 3/2) to very dark gray (5Y 3/1) color. Most of the sediment in this unit is stained to varying degrees by diagenetic hydrotroilite, which imparts an ephemeral black color (N2) to the

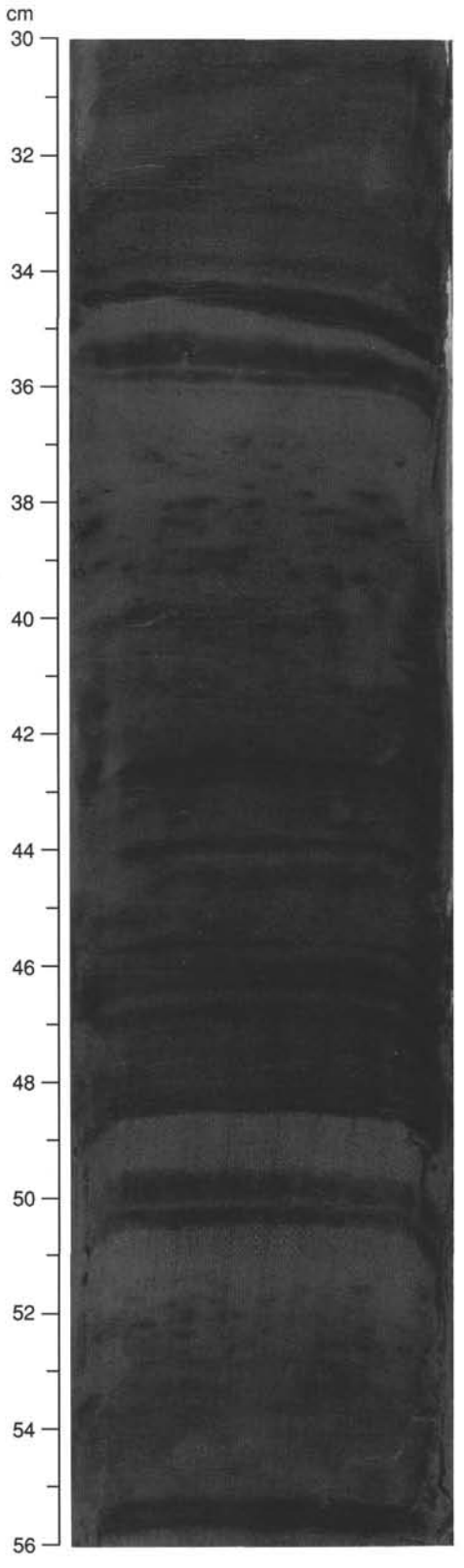

Figure 5. Black and dark gray (5Y 4/1) color banding in Subunit IIA (interval 155-934A-1H-3, 30–56 cm). The 3-cm-thick light-dark-light triplets at 49–52 cm and 35–38 cm are repeated at intervals of about 10–20 cm throughout Sections 155-934A-1H-2 and -3 (see whole-core photograph).

sediment as irregular patches and/or color bands (see "Introduction" chapter, this volume). Distinct color banding is visually striking at the top of the unit, but becomes subdued by 14.0 mbsf. The color banding is much more intense in Hole 934A than in 934B. Black hydrotroilite micronodules (1–2 mm diameter) are common in the lowest 5 m of the unit (Fig. 4). The carbonate content of Unit II is generally less than 3%, except in hemipelagic laminae at the tops of inferred turbidite muds (e.g., Sample 934A-5H-4, 58–59 cm, contains 19.7% carbonate). Unit II is divided into three subunits based on the frequency of common silt laminae, thin silt beds, and beds of sandy silt or fine silty sand (Figs. 3 and 4).

Subunit IIA

Subunit IIA extends from the base of Unit I to a depth of 7.70 mbsf (from 934A-1H-1, 93 cm, through -2H-3, 40 cm) and consists of dark olive gray (5Y 3/2) clay with black color banding on a scale from about 1 mm to several centimeters (Fig. 5). Subunit IIA contains only a few sharp-based silt laminae, stained black by hydrotroilite. The base of the subunit is placed at the top of the first thin sand bed in Hole 934A. A thin section from color-banded mud (Sample 934A-1H-3, 16–21 cm) shows that some of the primary lamination in the mud consists of sharp-based silty clay laminae (Fig. 6).

Subunit IIB

Subunit IIB extends from 7.70 to 37.89 mbsf (from 934A-2H-3, 40 cm, through -5H-4, 59 cm) and is characterized by silty clay with thin laminae of silt and beds of silty sand generally thinner than 5 cm, but in a few cases thicker than 1 m (Fig. 4). The silty clay is dark olive gray (5Y 3/2) to very dark gray (5Y 3/1) in color. Silt and sand layers have sharp bases and gradational tops. The average thickness and volumetric importance of silt and sand varies throughout the subunit (Fig. 4). Specifically, from 7.7 to 13.8 mbsf, the sediment is color banded and laminae and beds of silt and sand form less than 10% of the sediment, with bed thickness increasing toward the base. From 13.8 to 28.9 mbsf, sharp-based graded beds with basal grain sizes of fine sand to silt form about 50% of the sediment. These graded beds contain scattered fragments of wood larger than 1 cm (Fig. 7). From 28.9 to 37.9 mbsf, silt and sand layers form less than 10% of the section.

From 22.5 to 29.0 mbsf, there are several medium to thick beds that each grade from fine sand to silt. These beds locally contain abundant plant detritus. Primary lamination, if formed, was destroyed by the disruptive effects of gas expansion, except in a few cases (e.g., Fig. 8). As a result, these beds cannot be classified using the schemes of either Bouma (1962) or Lowe (1982). The thick, fine sand bed between 13.8 and 18.9 mbsf is unique relative to thin beds above and below. The actual thickness of this bed may be 50%–70% of the measured 5 m, based on the observation that the core liners in both the archive and working halves of Section 934A-3H-3 are not full and the sand has suffered significant gas expansion.

Subunit IIC

Subunit IIC extends from 37.89 to 42.30 mbsf (from 934A-5H-4, 59 cm, through -CC). The equivalent interval in Hole 934B is from 39.30 to 45.00 mbsf (from 934B-5H-3, 30 cm, through -6), but the subunit base is not as clear at Hole 934B as it is at Hole 934A. Subunit IIC consists of dark olive gray to very dark gray (5Y 3/1 to 5Y 3/2) silty clay without silt or sand layers. The sediment is slightly color banded and mottled. Micronodules of hydrotroilite, 1–2 mm in diameter, are extremely abundant, in sharp contrast to Subunit IIB.

Unit III

Intervals: 155-934A-6H-1 through -8H-3; 155-934B-5H-7 through -8H-3, 69 cm

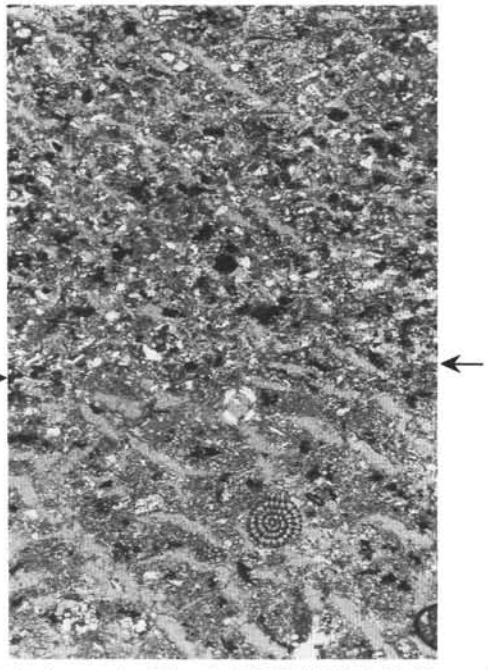

Figure 6. Photomicrograph of Sample 155-934A-1H-3, 16–21 cm, showing the sharp base of a silty clay turbidite (arrows) overlying homogeneous clay containing foraminifers. Elsewhere in the thin section, foraminifers are concentrated into current-sorted laminae. The largest angular quartz grain in the field of view measures 0.07 mm across. Numerous voids in the thin section were produced by freeze drying. The photomicrograph was taken with partially crossed nicols. Scale: 55 mm on photo = 0.5 mm.

Age: late Pleistocene
Depth: 42.30–64.56 mbsf

Unit III is characterized by interbedded dark olive gray (5Y 3/2) silty clay, silt laminae, and laminae to medium beds of sandy silt and very fine silty sand. All the sediment has been affected by the following styles of soft-sediment deformation: gentle to steep dipping beds (Fig. 9A); plastic folding of strata (Fig. 9B); injections of sand and mud; partial mixing of coarser and finer components, which are thought to have been originally in separate laminae and beds (Fig. 9C); and apparent homogenization of thick intervals (e.g., in the lower part of Core 934A-6H and throughout -7H; Fig. 9D). Unit III is interpreted as a rapidly emplaced mass-transport deposit.

Unit IV

Intervals: 155-934A-8H-4, 0 cm, through -11H-6, 79 cm; 155-934B-8H-3, 69 cm, through -11H-4, 27 cm
Age: late Pleistocene
Depth: 64.56–97.30 mbsf

Unit IV is formed mainly of medium (Fig. 10) to thick beds of fine to medium sand and coarse silt, with minor interbedded silty clay. There is an 18-m-thick interval of structureless sand in Hole 934B (Fig. 4), which contains scattered disoriented mud clasts (Fig. 11A, B). Several larger clasts are folded (Fig. 11C). The lower part of the 18-m-thick bed was recovered in Core 934B-9H, where the sediment contains pockets of 1–2 mm quartzose sand, some granules, rare fine pebbles as large as 0.5 mm in diameter, and a few 2-mm fragments of gastropod and bivalve shells (Fig. 11D). This very coarse sand was disturbed (?liquefied) during core retrieval, so that neither the primary fabric nor the possibility of scour surfaces between the deposits of successive flows (i.e., amalgamation surfaces) could be assessed. Much of Core 934A-10H consists of structureless sandy silt with thin silty clay interbeds. From 88.7 to 96.2 mbsf, several thick beds con-

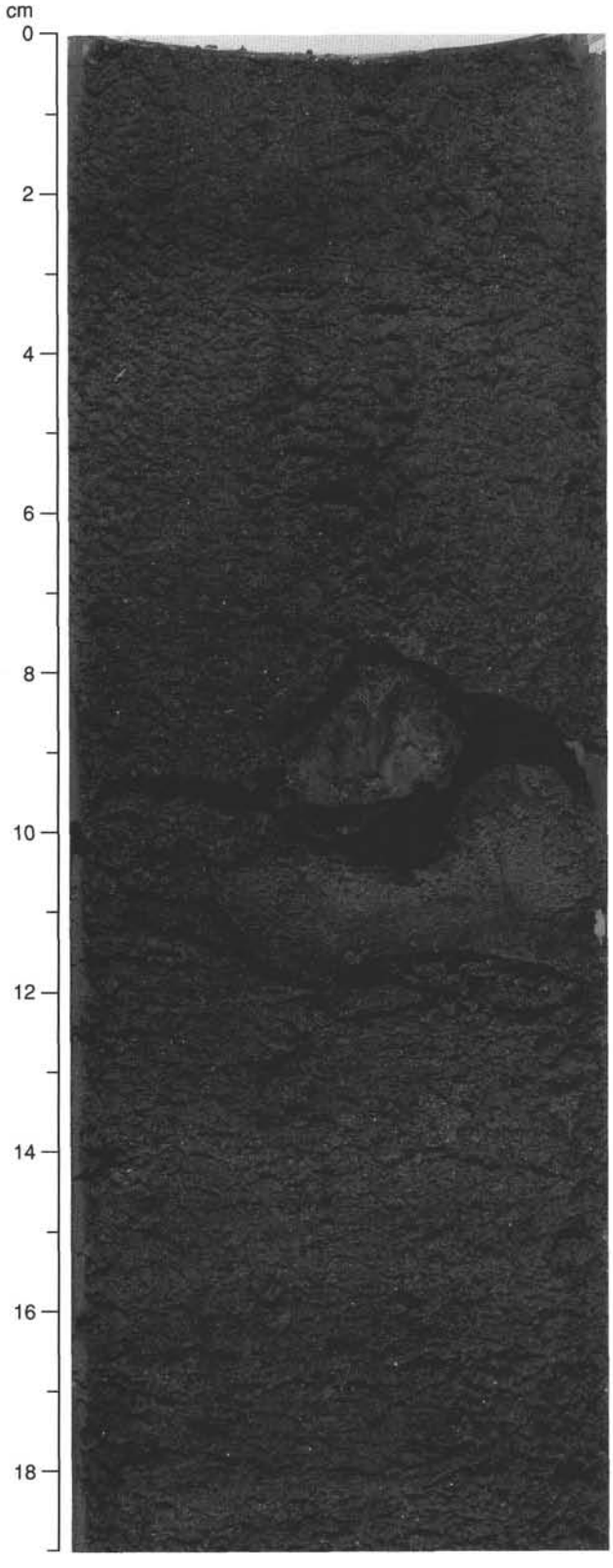

Figure 7. Fragment of soft wood (8–9 cm) in a fine micaceous sand in Subunit IIB (interval 155-934A-4H-3, 0–19 cm).

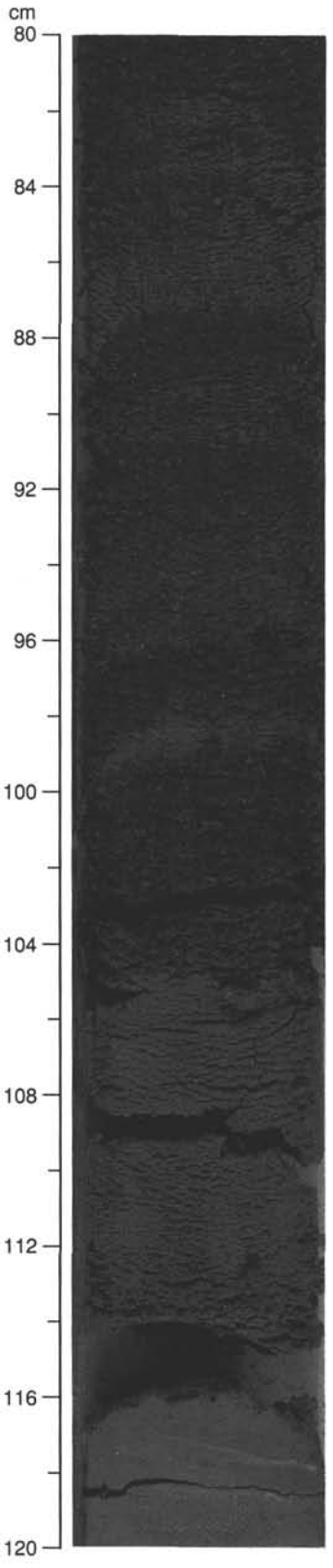

Figure 8. Crude stratification in a graded fine to very fine sandbed of Subunit IIB. The base of the bed is at 114 cm. The stratification is defined by variations in the content of organic detritus (interval 155-934A-4H-3, 80–120 cm).

tain 60%–70% mud clasts, as large as 35 cm in diameter, set in a sand matrix (Fig. 12). In general, grading is not apparent in these beds, but this might stem from partial to complete liquefaction that occurred during core handling (e.g., Core 934A-9H).

Unit V

Intervals: 155-934A-11H-6, 79 cm, through -12H-7, 57 cm
Age: late Pleistocene
Depth: 97.30–108.88 mbsf

Unit V consists mainly of thinly interbedded fine sand to coarse silt and silty clay. Silty clay forms about 30%–50% of the sediment. Except for two possible examples of ripple cross-lamination, primary structures were not visible in the gas-expanded silt and very fine sand beds. Several of these beds are thicker than 10 cm, even when allowances are made for gas expansion (see whole-core photograph of Core 934A-12H, "Cores" section, this volume).

Mineralogy

Mineralogy was determined by estimation of mineral volume percentages in smear slides and two thin sections of sand from Unit IV, and by X-ray diffraction (XRD) analysis.

Smear-slide Synthesis

The fine to very fine sand beds of Unit II consist of angular, fresh grains of 30%–50% quartz, 5%–20% feldspar, generally plagioclase, 5%–17% accessory minerals, and 4%–40% mica. The accessory minerals commonly include zircon, hornblende, augite, and opaques. Some sand beds in Cores 934A-3H and -4H contain about 10% each of plant detritus and accessory minerals. Fine to medium sand from the 18-m-thick sand deposit in Unit IV locally contains 25%–40% mica. Medium to coarse sand grains in this and other Unit IV sand beds are texturally distinct from the finer sand population, in that the coarse fraction is about 90% well-rounded quartz grains, some of which have surface coatings of iron oxide/hydroxide. Other minerals in the coarse fraction include K-feldspar, zircon, hornblende, augite, ?monazite, and opaque minerals.

Thin-section Sand Petrography

Two thin sections were made from sand in Core 934A-11H. The sand samples straddle the petrographic boundary between lithic arkoses and feldspathic litharenites. Sample 934A-11H-2, 10–12 cm, is a mixture of coarse to very fine sand (0.08–1.5 mm), with less than 10% silt. Quartz content is about 60%, feldspar about 15%, rock fragments about 15%, ferromagnesian minerals about 5%, and opaques about 5%. Quartz is mainly monocrystalline. Feldspar is mainly plagioclase but includes orthoclase and microcline. Ferromagnesian minerals include olivine (Fig. 13A), hornblende, and augite. Minor accessory minerals include euhedral and rounded zircon. The rock fragment component comprises particles of mafic to intermediate microlitic volcanic rock, glass shards, quartz-mica schist, and chert. One large biogenic-carbonate clast is present in the thin section. The silt and fine sand particles are angular to subangular, whereas about one half of the coarse particles, mainly quartz and K-feldspar, are rounded to subrounded (Fig. 13B); the rest are more angular. Many K-feldspar grains are slightly to moderately altered to phyllosilicates.

Sample 934A-11H-2, 24–26 cm, is fine to very fine sand. Quartz content is about 50%, feldspar about 15%, micas about 8%, ferromagnesian minerals about 10%, opaques about 3%, and rock fragments about 15%–20%. Quartz is both monocrystalline and polycrystalline. Feldspar is mainly plagioclase. Some K-feldspar grains are altered to phyllosilicate minerals (Fig. 13C). The rock fragment component includes particles of mafic to intermediate microlitic volcanic rock (Fig. 13D), glass shards, mica schist, and chert.

Ferromagnesian minerals include green and brown hornblende, augite, and ?glauconite. Minor accessory minerals include zircon. Most of the grains are angular to subangular. A small percentage of the coarsest grains are subrounded monocrystalline quartz.

XRD Data

A bulk XRD analysis was performed on five samples, including two calcareous clays from Unit I. The calcareous clays were digested in 0.5 N HCl to dissolve all biogenic calcite. Part of the remaining silicate fraction was run after air drying, and another part after heating to 550°C for 2 hr (see "Lithostratigraphy" section, "Explanatory Notes" chapter, this volume). The special study of Unit I was undertaken to compare its clay mineralogy with that of Pleistocene silty clays from other Leg 155 drill sites. Relative peak intensities for the five samples are listed in Table 2. Peak intensities for samples below Core 934A-1H are similar to Pleistocene samples from Sites 930 and 931, and will not be discussed.

There is no clear distinction between the clay minerals from foraminifer-nannofossil clays of Unit I and clay minerals that characterize the Pleistocene silty clays at Sites 930 and 931 (Table 2 of "Site 930" chapter and Table 2 of "Site 931" chapter, this volume). The average peak-intensity ratio smectite/[illite (+ mica)] for these Pleistocene silty clays is 0.53 at Site 930 and 0.50 at Site 931. Sample 934A-1H-1, 66–68 cm, has a slightly lower ratio of 0.42, whereas Sample 934A-1H-1, 21–23 cm, has a higher ratio of 0.68, resulting from a lower relative peak intensity for illite (+ mica).

Spectrophotometry

The high carbonate content of Unit I accounts for the strong reflection of visible light from this unit. Light reflectance in all wavelength bands from 400 to 700 nm never exceeds 25% in the dark sediment below Unit I. Changes in reflectance are caused mainly by color mottling and banding, and small-scale (millimeter to centimeter) partings produced by gas escape. The only feature of the reflectance data that can be attributed to changes in lithology is the ratio of red (650–700 nm) to blue (450–500 nm) reflectance (Fig. 3). The highest red/blue ratio correlates with the carbonate-rich Unit I. The enhanced reflectance of the red spectrum is caused by the high iron-oxyhydroxide content of Unit I, which also accounts for its brownish color.

Quartz grains in the levee sediment of Units II through V are commonly stained by iron oxides. The sensitivity of red-spectrum reflectance to traces of iron oxyhydroxides therefore enables the distinction of intervals rich in sand beds. Positive deviations from the average red/blue ratio can be attributed to the occurrence of sand beds in cores from 14 to 18 mbsf, 47 mbsf, and 58 mbsf in Hole 934A (Fig. 3). The first two peaks correspond to increases in magnetic susceptibility (see "Paleomagnetism" section, this chapter), which presumably are also related to enhanced iron-oxyhydroxide content of sand beds. The triple peak in the red/blue ratio near 47 mbsf in Hole 934A was also found at 51 mbsf in Hole 934B. From 70 to 100 mbsf, the red/blue ratio at Hole 934A has higher amplitude fluctuations than at Hole 934B. This amplitude difference is attributed to more abundant and thicker sand beds at Hole 934B (Fig. 4).

Discussion

A key element in the interpretation of the cored succession at Site 934 is the contorted slump deposit of Unit III. Below the slump, the succession is mainly sand and coarse silt. Above the slump, Subunit IIC is a mud drape within an apparent inactive channel segment. This relationship suggests that emplacement of the slump is associated with meander cutoff and subsequent abandonment of this part of the Amazon Channel. Either the slump itself partially filled this channel segment, causing diversion of turbidity currents across the narrow meander neck to the west, or the channel was initially plugged by the thick sand bed at the top of Unit IV. The emplacement of this sand bed may have undercut the banks of the channel, which led to subsequent failure of the levee margin to form Unit III.

The 18-m-thick sand, which is characterized by scattered meter-scale mud clasts, granules and pebbles of quartz, and friable clasts of silty sand (interval 934B-8H-3, 87–104 cm), may be a cohesionless debris-flow deposit, as defined by Postma (1986). In a cohesionless debris flow, grains are supported by excess pore pressures and buoyancy, and not by the strength of a clay matrix. Deposition from such a flow may have plugged the channel thalweg and triggered cutoff at the neck of the meander loop.

The sand and silt deposits of the lower part of Unit IV are interpreted as channel-floor deposits of the formerly active channel. These deposits rest on finer sediment of Unit V that may lie below an erosional surface at the base of the channel-fill sequence. The inferred channel-floor deposits of Unit IV are thought to have been emplaced by a succession of turbidity currents and cohesionless, sandy mass flows (e.g., debris flows, liquefied flows).

The top of the inferred channel-floor sequence is at a depth of about 80 mbsf (Fig. 4), which is 25 m below the depth of the modern floor of the Amazon Channel to the west (Fig. 1). If meander-loop abandonment indeed occurred at the time of emplacement of the 18-m-thick sand bed, then subsequent infilling of the topographically low abandoned channel by focused overbank flow (i.e., "flow stripping" of Normark et al., 1979) from the Amazon Channel neck cutoff could account for the present elevation difference between the floor of this meander loop and the floor of the Amazon Channel. The overspill events deposited either laminated silty clays (now color banded) or laminae and very thin beds of fine sand and silt (Subunits IIA and IIC), or thin to thick beds of silt and sand containing woody debris (Subunit IIB), depending on thickness and grain-size distribution of the suspended load of the turbidity currents. The thick bed of fine sand from 13.80 to 18.89 mbsf (Fig. 4) probably was deposited from an unusually large turbidity current, the top of which was trapped by topography after being "flow stripped" off into the abandoned meander loop.

As at all other Leg 155 sites, Holocene sea-level rise apparently accounts for the decrease of turbidites and increase in nannofossils and foraminifers in the upper part of Subunit IIA and through Unit I.

The sand types recovered at Site 934 have similar composition and texture to the sand types from the nearby Guiana Basin described by Damuth and Fairbridge (1970), except that samples from Site 934 appear to contain less feldspar. We agree with Damuth and Fairbridge (1970) in finding that medium to coarse quartz sand grains are commonly subrounded to well rounded. Fragments of microlitic volcanic rocks and the heavy minerals augite and olivine indicate a contribution from mafic extrusive rocks. These latter components are particularly labile, and could not have survived prolonged chemical weathering. Detrital micas and fragments of mica schist require that metamorphic rocks also contributed detritus to the load of the Pleistocene Amazon River.

BIOSTRATIGRAPHY

Calcareous Nannofossils

Nannofossils are abundant and well preserved only in the mudline, calcareous clay, Holocene-age samples. Samples taken every 10–20 cm between 0 and 1.4 mbsf show that the nannofossil assemblages are well preserved to a depth of 0.3 mbsf (Sample 934A-1H-1, 19–20 cm, Fig. 14). Below 0.3 mbsf the overall abundance of nannofossils decreases and the assemblage becomes less diversified (Sample 934A-1H-1, 39–40 cm). This reduction in abundance and diversity is unlikely to have been caused by dissolution because (1) the nannofossil preservation appears similar to that of the surface sample and (2) pteropods are present. All core-catcher samples of Hole 934A have low abundances or are barren of calcareous nannofossils (Table 3). In Sample 934A-5H-CC, 23–24 cm, a few specimens of the cold-

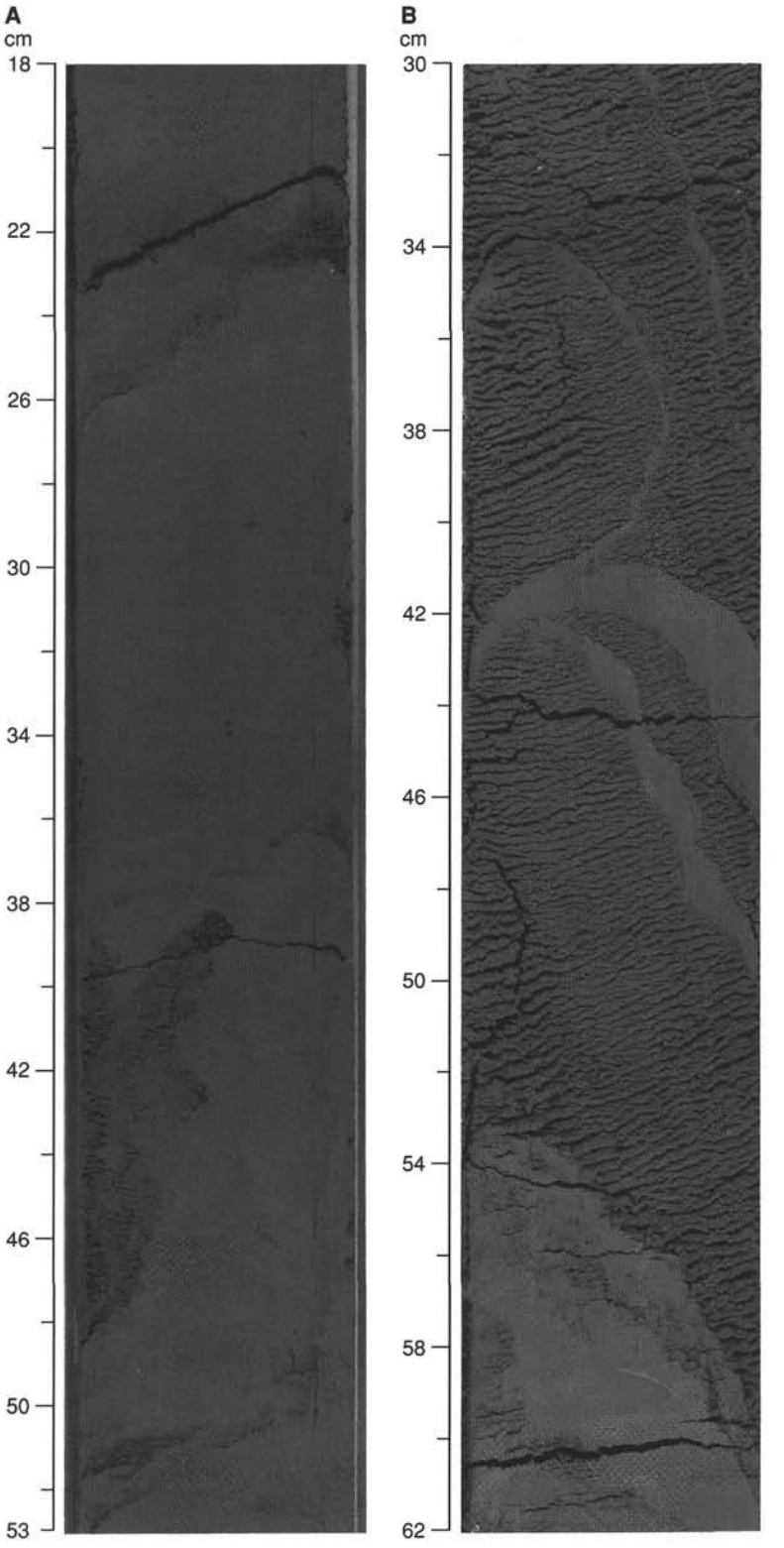

Figure 9. Soft-sediment deformation in Unit III. **A.** Tilted and deformed silt laminae and an irregular silt pocket (interval 155-934A-6H-2, 18–53 cm). **B.** Contorted silty clay laminae in a matrix of silty sand (interval 155-934A-7H-5, 30–62 cm). **C.** Deformed silty clay bands in a matrix of partially mixed silty clay and silt (interval 155-934B-6H-4, 10–40 cm). **D.** Remnants of silty clay laminae in an essentially homogenized matrix of silt-rich mud (interval 155-934B-6H-6, 12–44 cm).

water form *Coccolithus pelagicus* were present, indicating glacial conditions. Clasts of carbonate-rich sediment within the homogenous clay sequence of Unit IIB were barren of calcareous nannofossils (e.g., Sample 934A-5H-3, 30 cm).

Closely spaced samples were taken from Unit IIB (Hole 934A) to study the relationship between the abundance of calcareous nannofossils and turbidites (Table 3). Eight distinct turbidites are present in Section 934A-1H-2. One of these turbidites is capped by a 0.5-cm-thick tan clay. In the bottom of the overlying turbidite, nannofossils are very rare and poorly preserved (Sample 934A-1H-2, 125.8 cm). The tan clay itself has a diverse and well-preserved assemblage of late Quaternary age (Zone CN15b; Sample 934A-1H-2, 126.0 cm). The mottled clay immediately below the tan clay is characterized by a low abundance of poorly preserved nannofossils (Sample 934A-1H-2, 126.5 cm). The abundance and preservation of calcareous nannofossils deteriorate further in the underlying portion of the turbidite.

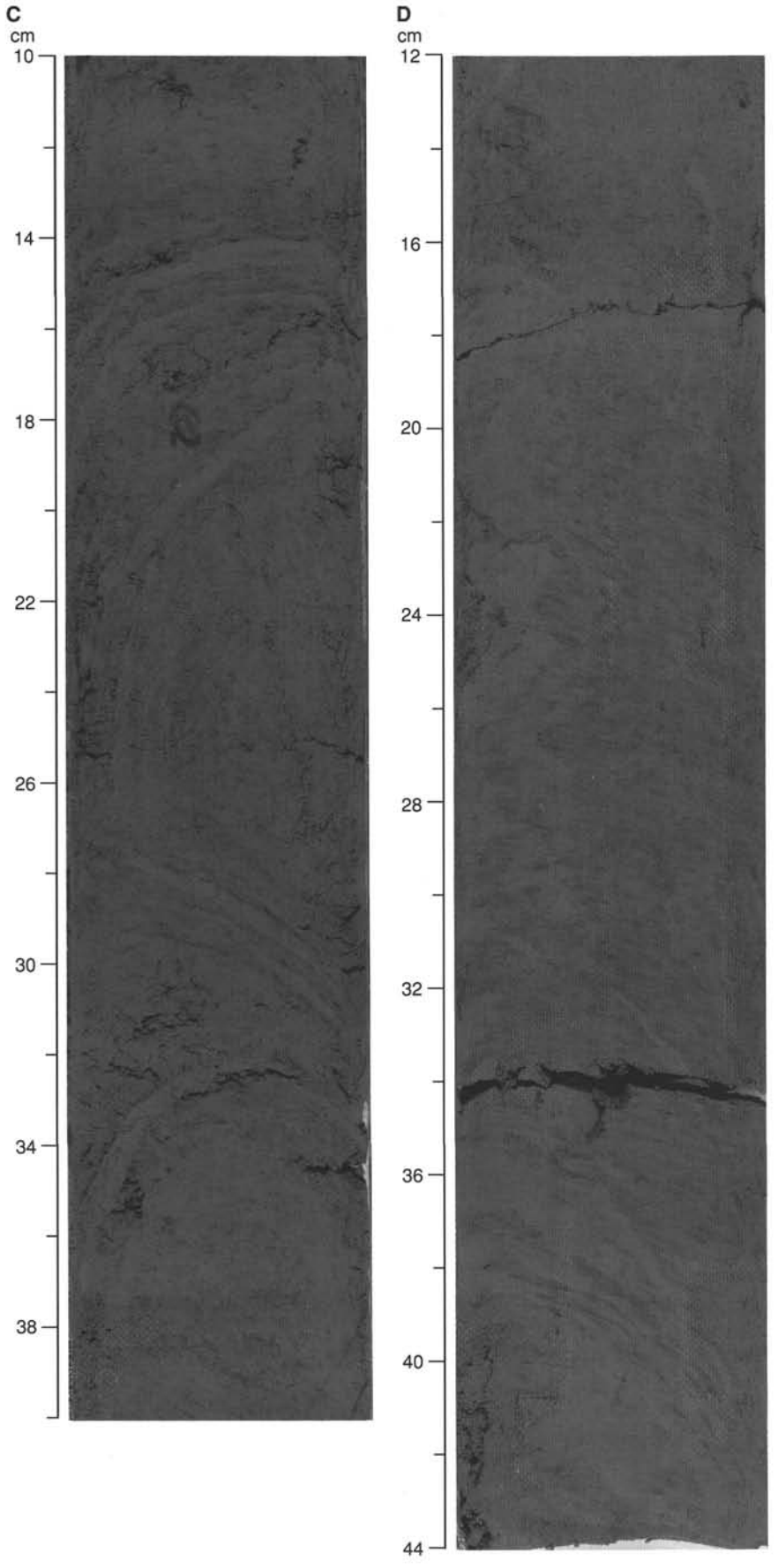

Figure 9 (continued).

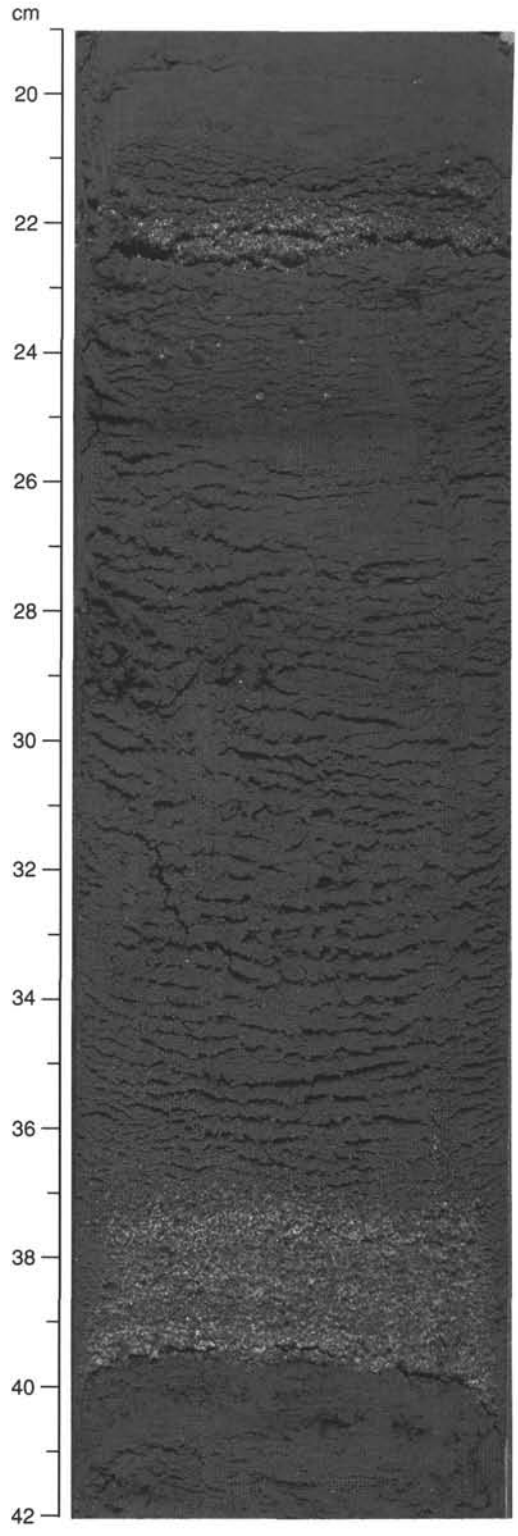

Figure 10. Sharp-based bed, graded from medium sand at the base (39.5 cm) to coarse silt at the top in Unit IV. The basal medium-sand division of this turbidite has subtle parallel lamination, but no other primary structures are visible, possibly because of disruption by gas expansion (interval 155-934A-10H-6, 19–42).

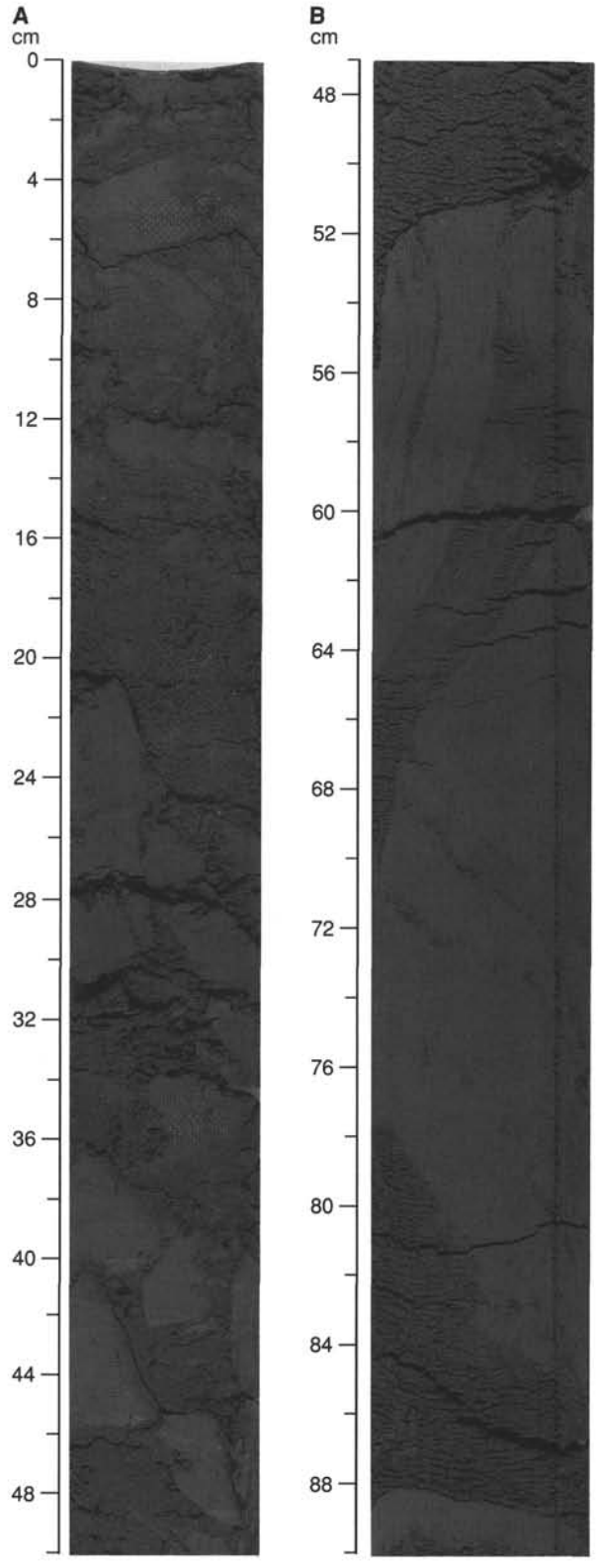

Figure 11. Features of the 18-m-thick sand unit of Unit IV. **A.** 1- to 10-cm-diameter soft mud clasts in a very fine sand matrix (interval 155-934B-8H-4, 0–50 cm). **B.** Very large mud clasts, with internal laminations that are tilted and contorted with respect to bedding in the cores; the streaky texture in the sand matrix at about 60 cm may indicate pore-water escape or sand injection upward between two clasts (interval 155-934A-11H-4, 47–90 cm).

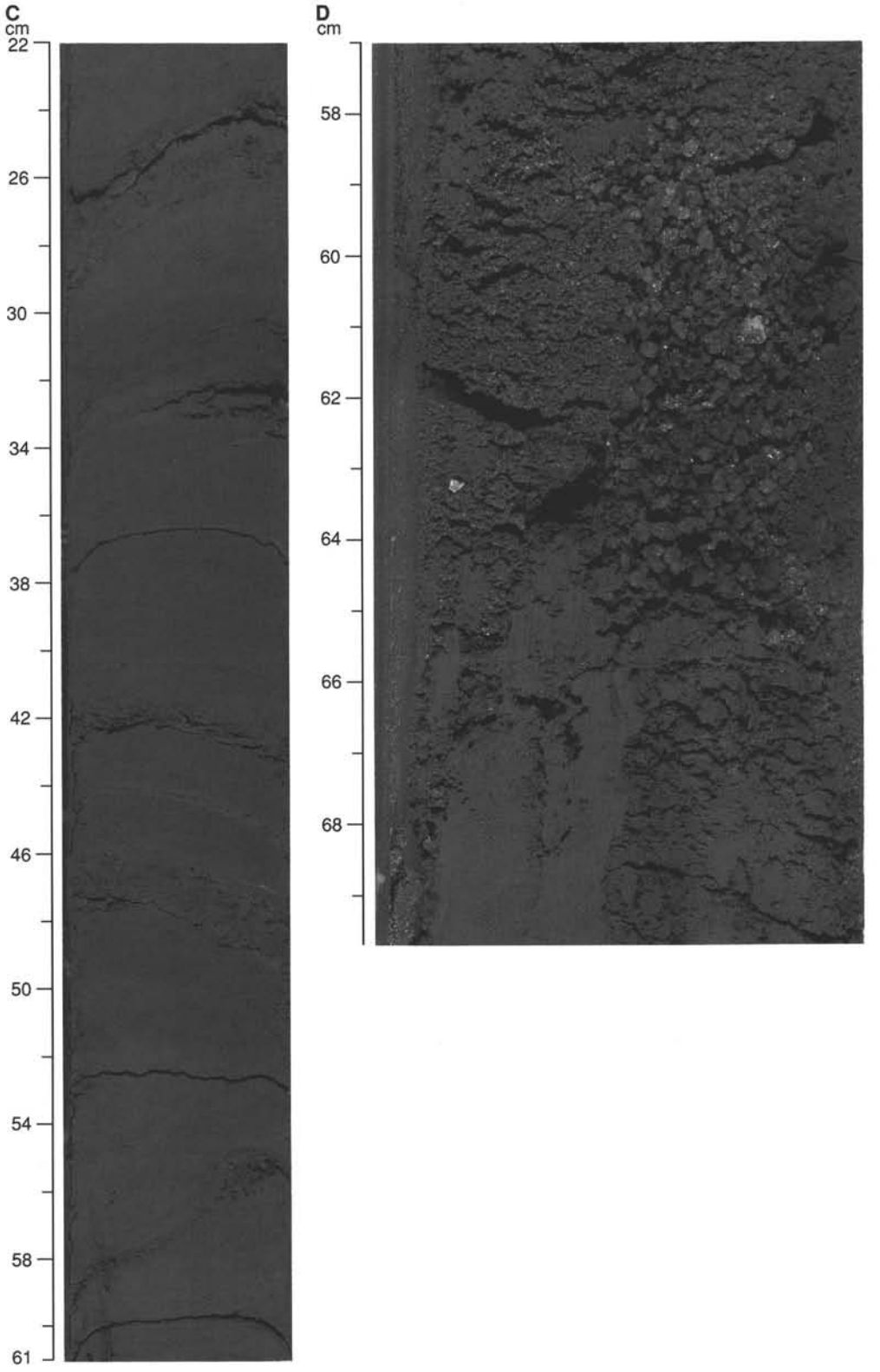

Figure 11 (continued). **C.** Folded, laminated clast of mainly silty clay (at about 75 mbsf in Fig. 4); a fold axis occurs at 53 cm (interval 155-934B-9H-2, 22–61 cm). **D.** Disturbed very coarse sand (interval 155-934B-9H-5, 57–69.7 cm).

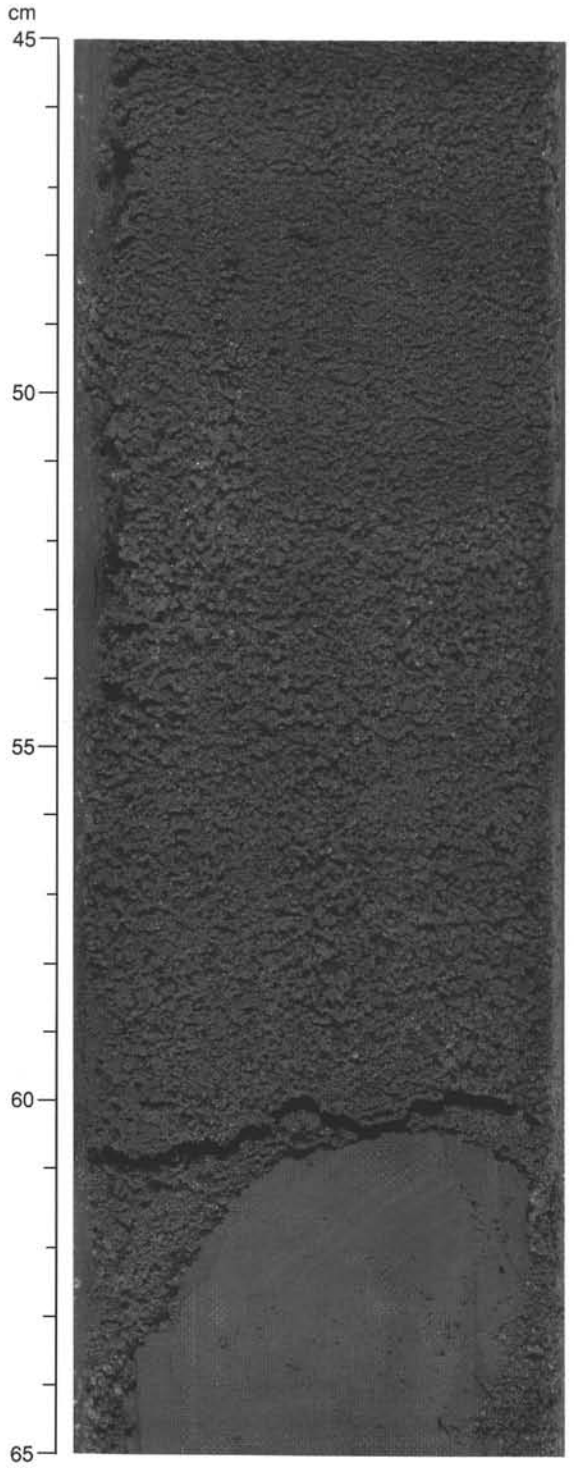

Figure 12. Fine to medium sand that characterizes very thick beds near the bottom of Unit IV. The silty clay at the base of the photograph is a mud clast (interval 155-934B-11H-1, 45–65 cm).

Nannofossils only reappear in the thin, tan clay layer at the top of the next turbidite downcore (Sample 934A-1H-2, 143.2 cm). The observed change in nannofossil abundances across turbidites may indicate that calcareous nannofossils are sorted during transportation and are deposited as the last component of the turbidite. Similar detailed surveys of the abundance of calcareous nannofossils across a number of other turbidites were made at Hole 934A (e.g., in Section 934A-5H-4) and did not show similar changes in abundance, which may be the result of lower nannofossil abundances below Unit I. The lack of a clear pattern within these turbidites may also be the result of rapid deposition of two consecutive turbidites, which might not allow the nannofossil-rich portion to settle before the next turbidite is deposited.

Planktonic Foraminifers

Ericson zones were assigned to sediment in Hole 934A (Table 4). The boundary between Ericson Zones Z and Y (disappearance of *G. menardii* and *G. tumida*) was initially placed between the mud-line Sample 934A-1H, 0 cm (0 mbsf), and Sample 934A-1H-CC, 5–14 cm (4.2 mbsf; Fig. 15). A high-resolution study was made to more precisely define the Z/Y boundary. Counts were made of the number of *G. menardii, G. tumida, G. fimbriata,* and the total number of planktonic foraminifers in a split of between 300 and 400 planktonic foraminifer tests (Table 5). The "rare" *G. menardii* and *G. tumida* found in Section 934A-1H-CC, 5–14 cm (4.2 mbsf, Fig. 14) are not in place, as they only appear in the core above 0.9 mbsf. This suggests that at least the first core catcher may have foraminifers that are washed down or trapped during coring. Counting results show that the appearance of *G. menardii, G. tumida,* and *G. fimbriata* is not coeval. *G. tumida* first appears at 0.9 mbsf, *G. menardii* at 0.4 mbsf, and *G. fimbriata* at 0.3 mbsf. This distribution is not an effect of dissolution as pteropods were also found (Table 5). The first occurrence offset of *G. menardii, G. tumida,* and *G. fimbriata* is due to their reappearance in the Atlantic Ocean at different times in the Holocene. Recent AMS ^{14}C dates indicate that *G. tumida* re-entered the North Atlantic 9,000 yr ago and did not reappear in the northeast Atlantic until 7,300 yr ago, and. *G. menardii* did not reappear in the Atlantic until 6,250 yr ago (G. Jones et al., WHOI, pers. comm., 1994). On the basis of these results we suggest that a working criteria of the Z/Y boundary should be the first appearance of *G. tumida.* Based on the results of this higher resolution study, the Z/Y boundary is placed between 0.9 and 1.2 mbsf. Foraminifers are rare or absent from 14.5 mbsf (934A-2H-CC, 25–34 cm) through 108 mbsf (934B-12H-CC, 0–9 cm), precluding any foraminifer zonation or dating of the sediment below 14.5 mbsf.

Benthic Foraminifers

Low abundances of upper- to mid-bathyal benthics (*Bulimina marginata* and *Bolivina* spp.) were found at 100 mbsf (934A-11H-CC, 30–39 cm), and at 108 mbsf (934A-12H-CC, 0–9 cm). The abyssal benthic foraminifers *Pyrgo* spp. were found in low abundance at 44 mbsf (934A-5H-CC, 24–33 cm).

Siliceous Microfossils

Site 934 is barren of diatoms, except for the mud-line sample where solution-resistant species of marine pelagic diatoms are present. Rare siliceous sponge spicules are present in the pre-Holocene section of Site 934 (Table 3). Fragments of radiolarians are present in the mud-line sample.

Palynology

Eight samples where examined from Hole 934A (Table 6). In general, low abundance and moderate preservation is characteristic. The assemblages tend to be dominated by monolete spores and are not diagnostic of specific terrestrial environments. *Mauritia* pollen, probably derived from the common swamp forest palm *Mauritia flexuosa,* was recorded in the upper Pleistocene section (Sample 934A-1H-2, 35–37 cm). Dinoflagellates were not found. Wood particles were observed in all microscope sample slides in varying abundance. Abundant organic material, including leaf fragments and intact seeds, was observed in Pleistocene core-catcher samples at 15–24 mbsf (Sam-

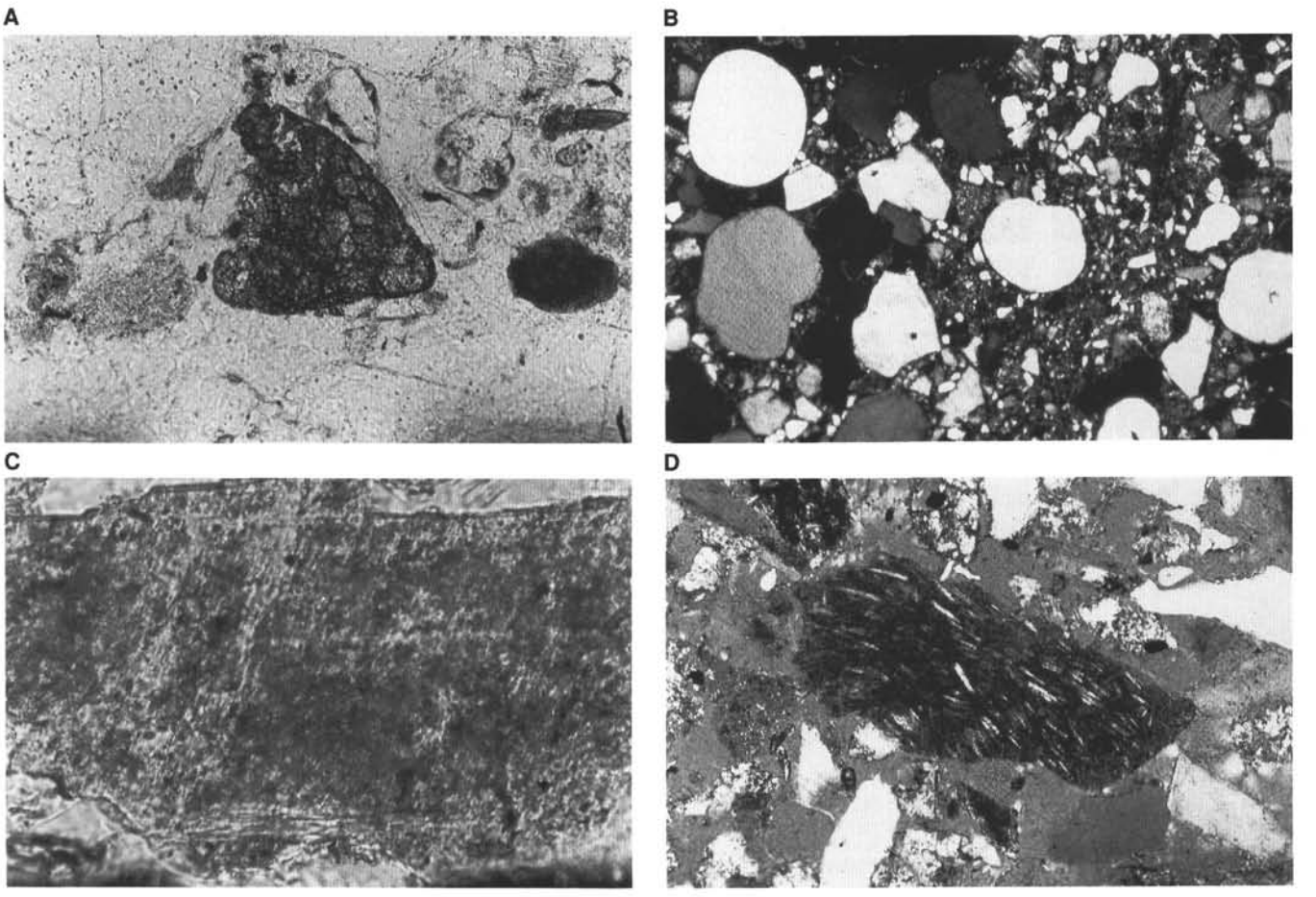

Figure 13. Photomicrographs of sand types from Unit IV. **A.** Olivine grain (center) in plane-polarized light. Scale: 86 mm on photo = 0.5 mm. (Sample 155-934A-11H-2, 10–12 cm) **B.** General view in cross-polarized light of sand in Sample 155-934A-11H-2, 10–12 cm, showing well-rounded quartz grains. Scale: 43 mm on photo = 1 mm. **C.** Altered angular K-feldspar grain in plane-polarized light. Scale: 69 mm on photo = 0.1 mm. (Sample 155-934A-11H-2, 24–26 cm) **D.** Microlitic volcanic rock fragment in partly cross-polarized light. Scale: 86 mm on photo = 0.5 mm. (Sample 155-934A-11H-2, 24–26 cm).

ples 934A-2H-CC, 25–34 cm, and -3H-CC, 18–27 cm) and 90–109 mbsf (Samples 934A-10H-CC, 0–9 cm, and -12H-CC, 0–9 cm).

Stratigraphic Summary

The first appearances of *G. menardii* and *G. tumida* occur at different depths in Hole 934A. We suggest a working definition of the Z/Y boundary as the first reappearance of *G. tumida*. The Z/Y boundary at Hole 934A is between 0.9 and 1.2 mbsf. The low abundance of microfossils below 14.5 mbsf prevents age determination from 14.5 mbsf to the bottom of the hole (108.9 mbsf). Palynomorphs are rare in Hole 934A, although wood fragments (>63 µm) are abundant in the upper Pleistocene at 15–24 mbsf and 90–109 mbsf.

PALEOMAGNETISM

Remanence Studies

All 23 APC cores from Holes 934A and 934B were measured on the pass-through cryogenic magnetometer. The Tensor tool was operational for 10 of the Hole 934A cores and five of the Hole 934B cores. Figures 16, 17, and 18 compare the azimuthally corrected declinations, inclinations, and remanence intensities between the two holes.

Declinations centered about 0° indicate that the Tensor tool continued to perform well at this site. Downhole counter-clockwise twisting of the APC cores was again indicated by uniform westerly

Table 2. Relative peak intensities of the main minerals in selected samples from Hole 934A.

Core, section, interval (cm)	Depth (mbsf)	Relative intensity of primary peaks								
		Smectite	Mica + Illite	Kaolinite	Quartz	Plagioclase	K-feldspar	Augite	Hornblende	Calcite
155-934A-										
1H-1, 21–23	0.21	12.4	18.3	14.8	100.0	14.8	13.2	3.5	*	*
1H-1, 66–68	0.68	5.9	13.9	7.1	100.0	6.6	6.1	3.2	*	*
4H-5, 136–137	29.66	13.1	24.4	12.4	100.0	11.4	4.5	1.9	*	*
9H-3, 65–66	74.19	18.5	37.7	23.2	100.0	9.3	*	3.0	*	*
10H-7, 54–55	89.84	16.1	34.0	18.7	100.0	9.8	3.9	2.6	*	*

Notes: See "Lithostratigraphy" section in the "Explanatory Notes" chapter, this volume, for XRD methods. * denotes non-detection.

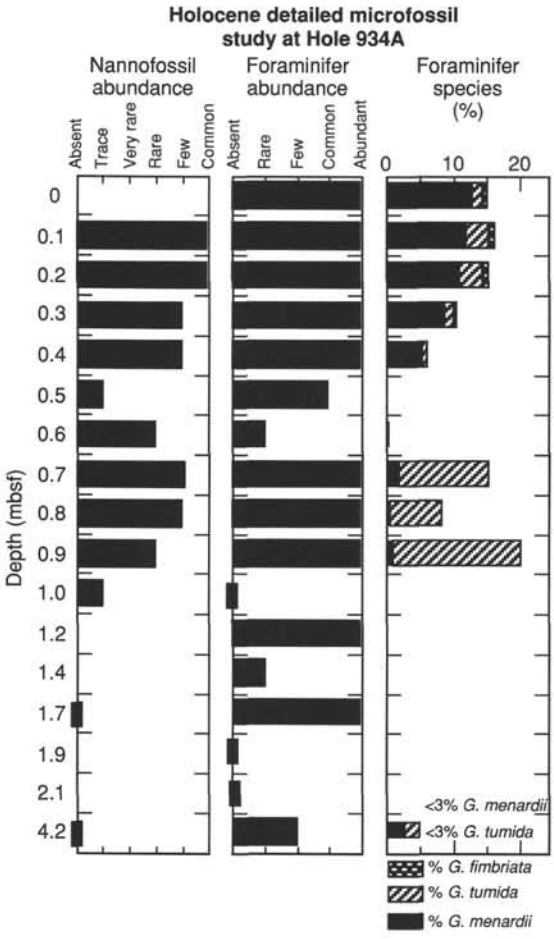

Figure 14. Relative abundances of *G. menardii*, *G. tumida*, and *G. fimbriata* in Core 934A-1H (0 to 4.2 mbsf).

rotation of intra-core declinations by up to 100°. This effect can create an illusion of secular variation, as declinations swing back and forth between values >0° and <0° (Fig. 16). However, comparison to the sub-bottom depths of the core intervals indicates that the sharp jumps to more easterly declinations correspond to breaks between cores.

Inclinations in Hole 934A are noticeably biased toward positive values, but above 45.5 mbsf in Hole 934B they are centered on 0°. This depth is near the top of lithostratigraphic Unit III, a rapidly emplaced mass-transport deposit in Hole 934B. Presumably drill stem magnetization remains a significant component of AF demagnetized remanence throughout this slump deposit in both holes, as well as in the overlying inactive channel deposits of Hole 934A. Two cycles of inclination oscillations (1 and 2 in Fig. 17), probably attributable to secular variation, can be discerned in the channel-deposited sediment.

Remanence intensities in both holes decrease from values of ~11 mA/m at the top of Unit IIA to a mean value of ~7 mA/m at just above mass-transport Unit III. Within Unit III (42.3 to 64.56 mbsf in Hole 934A), the mean intensities drop by another factor of two (Fig. 18). The underlying sediment displays highly variable remanence intensities, reflecting its interbedded clay/silt/sand character.

No geomagnetic excursions (i.e., the Lake Mungo Excursion) were observed in these holes, which is consistent with the assumed relatively young age (<30 ka) of these Amazon Channel deposits.

Magnetic Susceptibility

Whole-core and discrete-sample magnetic susceptibilities were measured on all the cores from Hole 934A. Only whole-core measurements were performed on the cores from Hole 934B. The results from Hole 934A were used to represent the whole-core variation except for a short interval from Hole 934B that was included to fill in a gap between about 75 to 83 mbsf (Fig. 19).

The lowest whole-core susceptibility values are associated with Unit I and Subunit IIC, a silty clay without silt or sand layers, whereas the highest values are within Subunit IIB and Units IV and V. In general, this site has susceptibility signals higher than those of previous sites, probably due to the coarser grained, poorly sorted nature of the channel deposits, as Site 934 was drilled into an abandoned channel meander.

ORGANIC GEOCHEMISTRY

Volatile Hydrocarbons

Headspace and vacutainer methane concentrations at Site 934 increase rapidly below the sediment surface to 55,410 and 203,546 ppm

Table 3. Calcareous nannofossil and siliceous microfossil abundance data for Hole 934A.

Core, section, interval (cm)	Top interval (mbsf)	Bottom interval (mbsf)	Calcareous nannofossils			Diatoms		Sponge spicules	Radiolarians	Ericson Zone (inferred from foraminifers)	Age (inferred from foraminifers)
			Abundance	Preservation	Zone	Marine	Freshwater				
155-934A-											
1H-MI, 0–0	0.00		a	g	CN15b	r	b	c	r	Z	Holocene
1H-2, 48	1.98		a	g						Y	late Pleist.
1H-2, 49	1.99		—	—						Y	late Pleist.
1H-2, 70	2.20		—	—						Y	late Pleist.
1H-2, 125	2.75		vr	—						Y	late Pleist.
1H-2, 125.8	2.76		vr	—						Y	late Pleist.
1H-2, 126	2.76		f	m						Y	late Pleist.
1H-2, 126.5	2.77		vr	—						Y	late Pleist.
1H-2, 130	2.80		tr	—						Y	late Pleist.
1H-2, 135	2.85		vr	—						Y	late Pleist.
1H-2, 140	2.90		vr	—						Y	late Pleist.
1H-2, 143	2.93		tr	—						Y	late Pleist.
1H-2, 143.2	2.93		f	p						Y	late Pleist.
1H-CC, 5–14	4.19	4.28	vr	—		b	b	r	b	Y	late Pleist.
2H-CC, 25–34	14.43	14.52	vr	—		b	b	b	b	Y	late Pleist.
3H-CC, 18–27	23.88	23.97	tr	—		b	b	b	b	—	?
4H-CC, 37–46	33.53	33.62	—	—		b	b	b	b	—	?
5H-CC, 24–33	43.93	44.01	vr	—		b	b	b	b	—	?
6H-CC, 24–33	52.42	52.51	tr	—		b	b	r	b	—	?
7H-CC, 38–47	61.56	61.66	tr	—		b	b	b	b	—	?
8H-CC, 32–41	71.73	71.82	b	—		b	b	b	b	—	?
9H-CC, 0–9	76.46	76.55	b	—		b	b	b	b	—	?
10H-CC, 0–9	90.16	90.25	b	—		b	b	b	b	—	?
11X-CC, 30–39	99.98	100.07	b	—		b	b	b	b	—	?
12X-CC, 0–9	108.88	108.97	b	—		b	b	b	b	RW	Pleist.

Table 4. Foraminifer abundance data for Hole 934A.

Core, section, interval (cm)	Top interval (mbsf)	Bottom interval (mbsf)	*Globorotalia menardii*	*Globorotalia tumida*	*Globorotalia tumida flexuosa*	*Pulleniatina obliquiloculata*	*Globigerinoides ruber* (white)	*Globigerinoides ruber* (pink)	*Globorotalia hexagonus*	*Neogloboquadrina dutertrei*	*Globorotalia trilobus trilobus*	*Globorotalia inflata*	*Globorotalia truncatulinoides*	*Globigerina bulloides*	*Globigerinoides trilobus sacculifer*	*Globorotalia fimbriata*	*Bolliella adamsi*	*Hastigerina digitata*	*Globigerina calida calida*	*Globorotalia crassaformis hessi*	*Globorotalia crassaformis viola*	*Globorotalia tosaensis*	*Orbulina universa*	Other planktonic foraminifers	Vivianite nodules	Overall foraminifer abundance	Preservation	Abundance of bathyal benthic foraminifers	Abundance of abyssal benthic foraminifers	Ericson Zone	Age
155-934A-																															
1H-MI, 0–0	0.00	0.00	C	R	B	R	F	R	R	C	C	B	B	B	C	F	B	R	B	B	B	B	B	B	B	A	G	B	B	Z	Holocene
1H-CC, 5–14	4.19	4.28	R	R	R	R	F	R	B	C	C	B	F	B	B	R	B	R	B	B	B	B	R	R	B	F	G	B	B	Y	late Pleist.
2H-CC, 25–34	14.43	14.52	B	B	B	R	C	B	B	A	A	B	C	B	B	B	B	B	B	B	B	B	B	B	R	R	M	B	B	Y	late Pleist.
3H-CC, 18–27	23.88	23.97	B	B	B	B	B	B	B	B	B	B	B	B	B	B	B	B	B	B	B	B	B	B	R	B	P	B	B	—	?
4H-CC, 37–46	33.53	33.62	B	B	B	C	C	R	B	C	F	B	F	B	F	B	B	B	B	B	B	B	B	B	C	F	M	B	B	—	?
5H-CC, 24–33	43.93	44.01	B	B	B	C	F	B	B	C	F	B	C	B	B	B	B	B	B	B	B	B	B	B	C	R	M	R	B	—	?
6H-CC, 24–33	52.42	52.51	B	B	B	R	B	B	B	B	B	B	B	B	B	B	B	B	B	B	B	B	B	R	C	B	P	B	B	—	?
7H-CC, 38–47	61.56	61.66	B	B	B	B	B	B	B	B	B	B	B	B	B	B	B	B	B	B	B	B	B	B	F	B	P	B	B	—	?
8H-CC, 32–41	71.73	71.82	B	B	B	B	B	B	B	B	B	B	B	B	B	B	B	B	B	B	B	B	B	B	C	B	P	B	B	—	?
9H-CC, 0–9	76.46	76.55	B	B	B	B	B	B	B	B	B	B	B	B	B	B	B	B	B	B	B	B	B	B	R	B	P	B	B	—	?
10H-CC, 0–9	90.16	90.25	B	B	B	B	B	B	B	B	B	B	B	B	B	B	B	B	B	B	B	B	B	B	R	B	P	B	B	—	?
11H-CC, 30–39	99.98	100.07	B	B	B	B	B	B	B	B	R	B	B	B	B	B	B	B	B	B	B	B	B	B	R	B	M	B	F	—	?
12H-CC, 0–9	108.88	108.97	B	B	B	B	B	B	B	R	R	B	B	B	R	B	B	B	B	B	B	B	B	B	B	R	P	B	R	RW	Pleist.

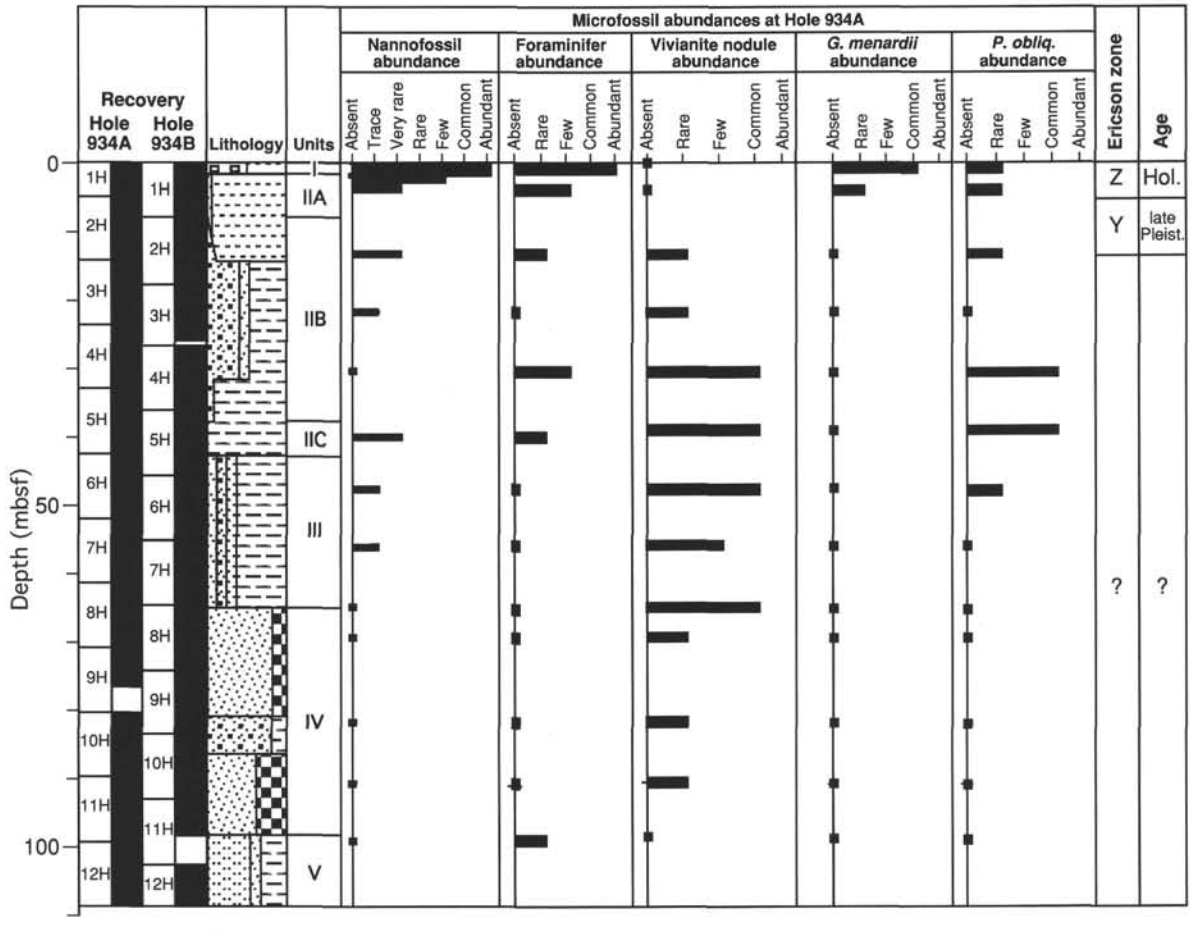

Figure 15. Biostratigraphic summary for Site 934.

Table 5. Relative abundance data of *G. menardii*, *G. tumida*, and *G. fimbriata* between 0 and 4.2 mbsf for Hole 934A.

Core, section interval (cm)	Top interval (mbsf)	Bottom interval (mbsf)	*G. menardii* (%)	*G. tumida* (%)	*G. fimbriata* (%)	Foram. abundance	Nanno. abundance	Pteropods
155-934A-								
1H, 0–2	0	0.2	12.5	1.7	0.7	A		none
1H, 8–10	0.08	0.1	11.7	3.4	0.8	A	A	none
1H-1, 18–20	0.18	0.2	10.5	3.7	0.9	A	A	none
1H-1, 28–30	0.28	0.3	8.3	1.5	0.5	A	C	none
1H-1, 38–40	0.38	0.4	5	1	0	A	C	none
1H-1, 48–50	0.48	0.5	0	0	0	C	Tr	none
1H-1, 58–60	0.58	0.6	0	0.3	0	R	F	present
1H-1, 68–70	0.68	0.7	1.5	13.7	0	A	F	present
1H-1, 78–80	0.78	0.8	0.3	7.8	0	A	C	none
1H-1, 88–90	0.88	0.9	0.6	19.4	0	A	F	present
1H-1, 98–100	0.98	1.0					Tr	
1H-1, 118–120	1.18	1.2	0	0	0	A		present
1H-1, 138–140	1.38	1.4	0	0	0	R		none
1H-1, 168–170	1.68	1.7	0	0	0	A	B	none
1H-1, 188–190	1.88	1.9	0	0	0	B		none
1H-1, 208–210	2.08	2.1	0	0	0	B		none
1H-CC, 5–15	4.27	4.29	<3.0	<3.0	0	F	B	present

Table 6. Palynomorph abundance and type data for Hole 934A.

Core, section, interval (cm)	Top interval (mbsf)	Bottom interval (mbsf)	Pollen and spores			Dinocysts	Wood/ carbonized particles	Ericson Zone (inferred from forams.)	Age (inferred from forams.)
			Abundance	Preservation	Major types recorded				
155-934A-									
1H-1, 35–37	0.35	0.37	b			b	r	Z	Holocene
1H-2, 35–37	1.85	1.87	r	p	*Mauritia*	b	f	Y	late Pleist.
1H-3, 79–81	3.79	3.81	f	g	TCP, monolete (psilate) spore	b	f	Y	late Pleist.
2H-1, 69–71	4.99	5.01	r	m	Monolete (psilate) spore	b	c	Y	late Pleist.
2H-5, 77–79	11.07	11.09	b			b	a	Y	late Pleist.
4H-4, 48–50	28.28	28.30	b			b	a	—	?
6H-2, 86–89	44.66	44.69	r	g	TCP	b	c	—	?
11H-CC, 39–40	100.07	100.08	r	m	Monolete (psilate) spore	b	a	—	?

Note: TCP = tricolporate

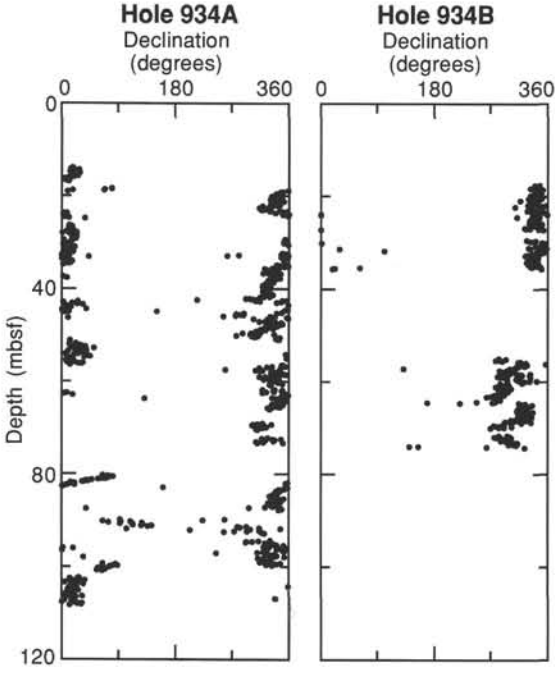

Figure 16. Declination for all azimuthally corrected (via Tensor tool) archive-half APC cores from Holes 934A and 934B. AF demagnetization level was 20 mT.

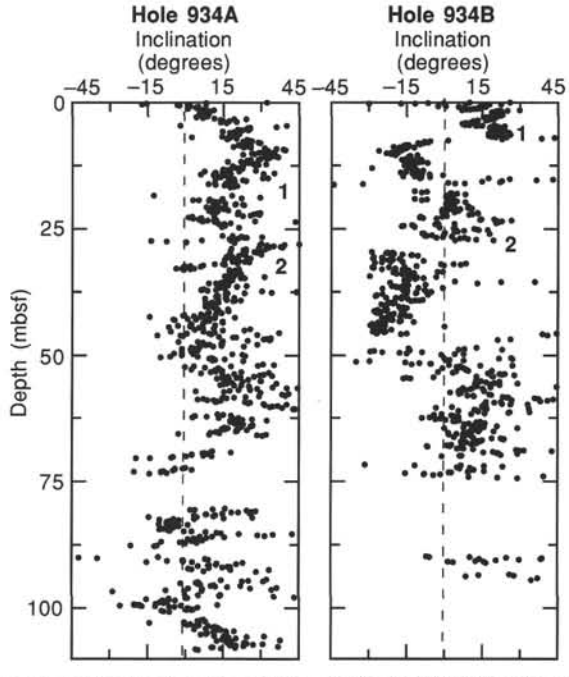

Figure 17. Inclination for all measured archive-half (APC) core sections from Holes 934A and 934B. Inclination cycles have been numbered 1 and 2 in both holes. AF demagnetization level was 20 mT.

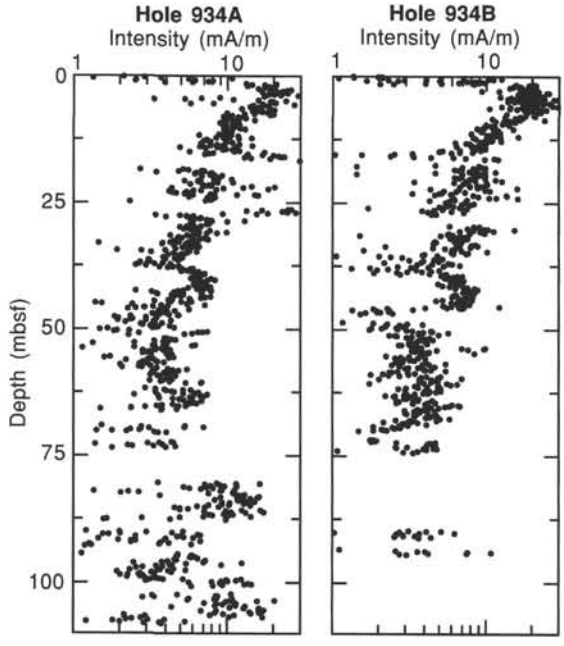

Figure 18. Remanence intensity for all measured archive-half (APC) cores from Holes 934A and 934B. AF demagnetization level was 20 mT.

at 11.80 mbsf (Table 7; Fig. 20). Below this depth, headspace methane concentrations decrease rapidly to 7400 ppm at 21.30 mbsf and range from 4800 to 17,400 ppm downhole. Vacutainer methane concentrations range from 149,398 to 944,071 ppm downhole. As at previous sites, vacutainer methane values are much higher than headspace concentrations (Fig. 20). Higher-molecular-weight hydrocarbons were not detected, indicating a predominantly biogenic methane source at Site 934.

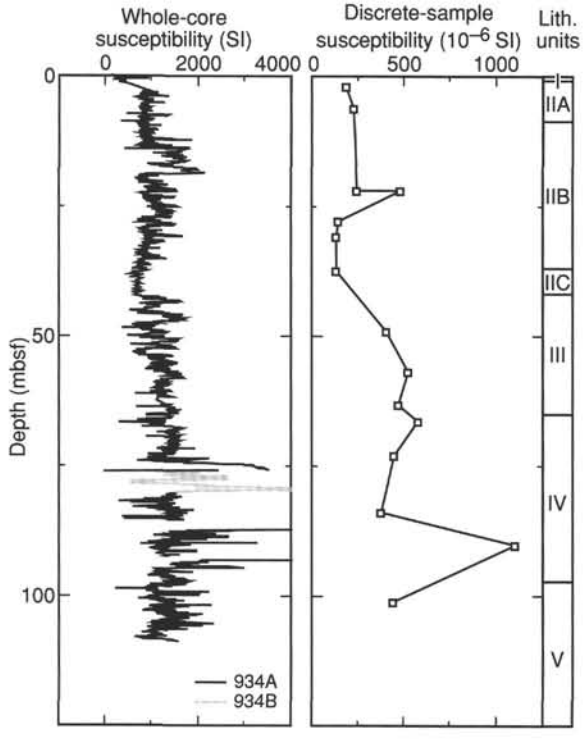

Figure 19. Magnetic susceptibility data for Site 934.

Table 7. Gas concentrations in sediments from Site 934.

Core, section, interval (cm)	Depth (mbsf)	Sed. temp.* (°C)	Methane HS (ppm)	Methane VAC (ppm)
155-934A-				
1H-2, 0–5	1.50	2	3	
2H-6, 0–5	11.80	3	55,410	203,546
3H-6, 0–5	21.30	3	7,434	438,570
4H-6, 0–5	30.80	3	7,269	922,541
5H-6, 0–5	40.30	4	8,426	149,398
6H-7, 0–5	50.47	4	7,578	495,235
7H-6, 0–5	59.30	5	12,513	902,103
8H-7, 0–5	69.06	5	4,832	720,480
9H-2, 0–5	72.30	5	8,556	944,071
10H-4, 0–5	84.80	5	13,128	681,629
11H-6, 0–5	97.30	5	17,443	931,373
12H-4, 0–5	103.80	5	7,411	

Notes: HS = Headspace; VAC = Vacutainer. Geothermal gradient = 45°C/km. Bottom-water temperature = 2°C. *See "In-situ Temperature Measurements" section, this chapter.

Carbon, Nitrogen, and Sulfur Concentrations

Carbonate, calculated as $CaCO_3$, concentration is 45.8% in the top sample at 0.63 mbsf (Table 8; Fig. 21). Carbonate decreases to 2.2% at 3.67 mbsf and remains fairly low (<4%) throughout the rest of Hole 934A, except for two elevated values at 37.88 mbsf (19.7%) and 40.88 mbsf (5.2%).

TOC concentrations are low (<0.2%) in the carbonate-rich sample at 0.63 mbsf and also in a sand-rich sample near the bottom of Hole 934A (105.33 mbsf). Most of the samples in Hole 934A have TOC concentrations between 0.8% and 1.1%, with one higher concentration (~1.4%) found at 63.77 mbsf. Relatively high concentrations of both carbonate (~20%) and TOC (~1%) were measured in Sample 934A-5H-4, 58–59 cm. This interval corresponds to a carbonate-rich lamina with abundant foraminifer fragments. At previous sites, all samples with carbonate contents higher than 15% exhibit significantly lower TOC concentrations.

Total nitrogen concentrations vary little throughout Hole 934A, with most values between 0.08% and 0.16%, and show a similar profile to TOC (Fig. 21). In a sandy sample (Sample 934A-12H-5, 3–4 cm) TN concentration is below the detection limit. The TS concentration profile is different from those of previous sites; concentrations in the top 29 mbsf range between 0% and 0.16%. Below this depth no sulfur was detected (Fig. 21).

Atomic ratios of organic carbon to total nitrogen, [C/N]a, are low at 0.63 mbsf. Below this depth, they increase to values between 7 and

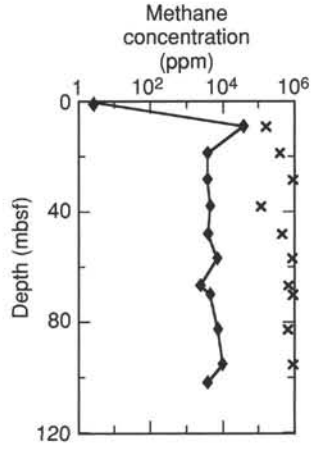

Figure 20. Methane concentrations (ppm) at Site 934. Headspace (diamonds) and vacutainer (×) samples are plotted.

Table 8. Elemental and organic carbon compositions of sediments from Site 934.

Core, section, interval (cm)	Depth (mbsf)	IC (%)	$CaCO_3$* (%)	TC (%)	TOC (%)	TN (%)	TS (%)	[C/N]a	Lith. unit
155-934A-									
1H-1, 63–64	0.63	5.50	45.8	5.69	0.19	0.11	0.00	2	I
1H-3, 67–68	3.67	0.27	2.2	1.11	0.84	0.13	0.14	8	
1H-3, 70–71	3.70	0.15	1.2	1.15	1.00	0.12	0.06	9	
1H-3, 72–73	3.72	0.01	0.1	0.97	0.96	0.14	0.16	8	
2H-4, 133–134	10.13	0.34	2.8	1.38	1.04	0.15	0.00	8	
2H-4, 138–139	10.18	0.33	2.7	1.34	1.01	0.13	0.05	9	
2H-4, 29–30	9.09	0.14	1.2	1.02	0.88	0.14	0.12	7	II
2H-5, 28–29	10.58	0.18	1.5	1.04	0.86	0.11	0.07	9	
3H-4, 82–83	19.12	0.34	2.8	1.38	1.04	0.16	0.08	8	
4H-4, 118–119	28.98	0.24	2.0	1.25	1.01	0.16	0.05	8	
4H-6, 29–30	31.09	0.21	1.7	1.20	0.99	0.13	0.00	9	
5H-4, 58–59	37.88	2.37	19.7	3.32	0.95	0.12	0.00	9	
5H-6, 58–59	40.88	0.62	5.2	1.71	1.09	0.15	0.00	9	
6H-3, 50–51	45.80	0.17	1.4	0.98	0.81	0.09	0.00	11	
6H-6, 50–51	49.47	0.00	0.0	0.92	0.92	0.09	0.00	12	
7H-3, 49–50	55.29	0.21	1.7	1.02	0.81	0.11	0.00	9	III
7H-6, 49–50	59.79	0.18	1.5	1.10	0.92	0.12	0.00	9	
8H-3, 64–65	63.77	0.20	1.7	1.54	1.34	0.10	0.00	16	
8H-5, 119–120	67.25	0.43	3.6	1.08	0.65	0.11	0.00	7	
9H-2, 49–50	72.79	0.18	1.5	0.79	0.61	0.08	0.00	9	IV
12H-5, 3–4	105.33	0.07	0.6	0.18	0.11	0.00	0.00		
12H-7, 14–15	108.44	0.19	1.6	0.98	0.79	0.11	0.00	9	V

*Calculated assuming all IC is calcite.

12. A spike in the [C/N]a ratio (16) was found at 63.77 mbsf, in a zone of sand and silty clay containing plant fragments.

INORGANIC GEOCHEMISTRY

Interstitial Water Analysis

Interstitial water samples were collected from seven sediment samples at Hole 934A. Samples were taken approximately every 10 m for the upper 40 mbsf and approximately every 40 m thereafter (Table 9 and Fig. 22). Salinities of the water samples range from 32.5 to 35.0 (Fig. 22A). In the upper 20 m of the hole, salinity decreases from 35.0 to 32.5. Below 21.25 mbsf, salinity varies between 32.5 and 33. Chloride concentrations rise from 551 to 561 mM over the first 20 m of the hole (Fig. 22B). Below 21.25 mbsf, the values are relatively constant, varying between 562 and 563 mM. Pore-water pH ranges from 7.50 to 7.77 (Fig. 22C) and shows no downhole trend. Pore-water alkalinity ranges from 6.28 to 16.99 mM. In the uppermost 30 m, alkalinity increases from 6.28 at 1.45 mbsf to 16.99 at 7.95 mbsf, and then decreases to 8.80 mM at 30.70 mbsf (Fig. 22D). Below 30.70 mbsf, alkalinity remains relatively constant, ranging from 9.67 to 6.93 mM. Dissolved magnesium and calcium concentrations decrease quickly over the upper 7.95 mbsf; values fall from seawater concentrations to around 40 and 5 mM, respectively (Fig. 22E and F). Below 7.95 mbsf, the values are quite constant, with less than 1 mM variation in either. Pore-water sulfate concentrations decrease rapidly over the upper 8 m. The concentration is 23.35 mM at 1.45 mbsf and has fallen to zero by 7.95 mbsf. The values remain zero downhole (Fig. 22G). Ammonium concentrations increase with depth from 0.66 mM at 1.45 mbsf to 6.97 mM at 40.20 mbsf (Fig. 22H). Below 40.20 mbsf, the ammonium concentration decreases slightly to 5.94 mM at 97.20 mbsf.

Pore-water phosphate concentrations are comparatively low throughout the hole, with values ranging from 2.6 to 18.0 µM (Fig. 22I). At all other sites a sharp maximum in phosphate concentration was observed at about 5 mbsf. It is likely that this sharp peak in concentration was missed due to the wide sampling interval. Dissolved silica concentrations vary from 301 to 434 µM. No depth trend is evident (Fig. 22J). Dissolved potassium concentrations decrease sharply from 12.1 mM at 1.45 mbsf to 7.9 mM at 7.95 mbsf (Fig. 22K). Thereafter, the concentration is relatively constant, varying between 6.7 and 7.6 mM. Pore-water sodium concentrations are quite constant throughout the hole, ranging from 471 to 475 mM (Fig. 22L). Dissolved iron concentrations are 32.5–10.4 µM between 1.45 and 21.25 mbsf (Fig. 22M). Concentrations increase to 95.2–109.6 µM between 30.70 and 68.96 mbsf, and then decrease to 49.8 µM near the bottom of the hole. Manganese concentrations are 24.5 µM at 1.45 mbsf, and then decrease to around 5 µM throughout the rest of the hole (Fig. 22N).

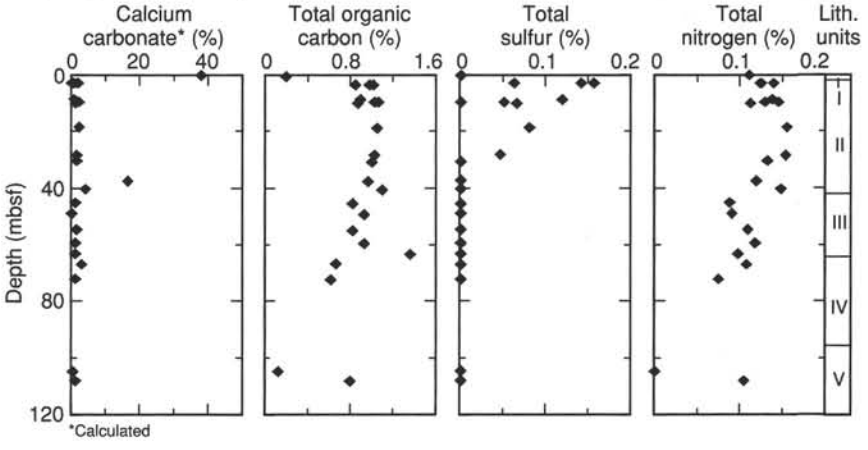

Figure 21. Concentration profiles of calcium carbonate, total organic carbon, total sulfur, and total nitrogen in Hole 934A.

Table 9. Interstitial water chemistry, Site 934.

Core, section, interval (cm)	Depth (mbsf)	Salinity	pH	Alkalinity (mM)	Cl^- (mM)	Mg^{2+} (mM)	Ca^{2+} (mM)	K^+ (mM)	HPO_4^{2-} (μM)	SO_4^{2-} (mM)	NH_4^+ (mM)	H_4SiO_4 (μM)	Na^+ (mM)	Fe^{2+} (μM)	Mn^{2+} (μM)
155-934A-															
1H-1, 145–150	1.45	35.0	7.50	6.28	551	48.6	9.7	12.1	7.4	23.35	0.66	301	475	32.5	24.5
2H-5, 145–150	7.95	33.5	7.77	16.99	555	40.3	5.1	7.9	9.3	0	3.63	401	473	26.2	4.0
3H-5, 145–150	21.25	32.5	7.61	12.20	561	41.3	4.7	7.5	2.6	0.03	5.00	350	474	10.4	5.5
4H-5, 140–150	30.70	32.5	7.51	8.80	562	40.7	4.9	7.2	6.9	0.03	5.20	399	473	95.2	5.0
5H-5, 140–150	40.20	32.5	7.68	9.19	563	41.6	4.1	6.7	3.7	0.04	6.97	356	474	109.6	6.0
8H-6, 140–150	68.96	33.0	7.51	9.67	562	41.4	4.8	7.3	18	0	6.17	434	472	110.4	6.2
11H-5, 140–150	97.20	32.5	7.56	6.93	563	41.1	4.7	7.6	3.4	0	5.94	247	471	49.8	8.5

Sediment Geochemistry

Two muds were sampled for major- and trace-element geochemistry (Tables 10 and 11) at depths of 12.20 mbsf and 67.17 mbsf, to test for possible compositional differences between channel sediment (this site) and levee deposits (previous sites). Mud compositions are indistinguishable from muds sampled at other sites, with SiO_2 of 66 and 62 wt%, and Al_2O_3 of 19 and 22 wt%. Alumina normalized ratios are similar to those at previous sites.

PHYSICAL PROPERTIES

Index Properties

Index properties were determined for all lithologic units in Hole 934A (Table 12). Water content values show an overall decrease with depth from 59% just below the seafloor to 24% at the base of the hole (Fig. 23). The single measurement from Unit I is 50.5%. Water contents decrease rapidly in the upper meter of Unit II, from 58% to 41%. Below 2 mbsf, water content gradually decreases in an undulating manner to 29% at 62 mbsf. The low values between 14 and 18 mbsf (Fig. 23) are in sand-rich beds. These values are most likely unrepresentative of in-situ conditions as a consequence of pore-water drainage prior to sampling. Below 62 mbsf, water content values of clayey sediment are more widely scattered and decrease from 30% to 23%. The common sand layers may account for this increased variability.

The porosity and wet-bulk density profiles show fluctuations similar to those of the water content profile (Fig. 23). From 2 to 13 mbsf there is little change in wet-bulk density, but below the sandy interval between 14 and 18 mbsf, wet-bulk densities gradually increase to 1.78 g/cm^3 at 42 mbsf. A distinct increase in wet-bulk density occurs at the boundary between Units II and III (42.30 mbsf). Unit III den-

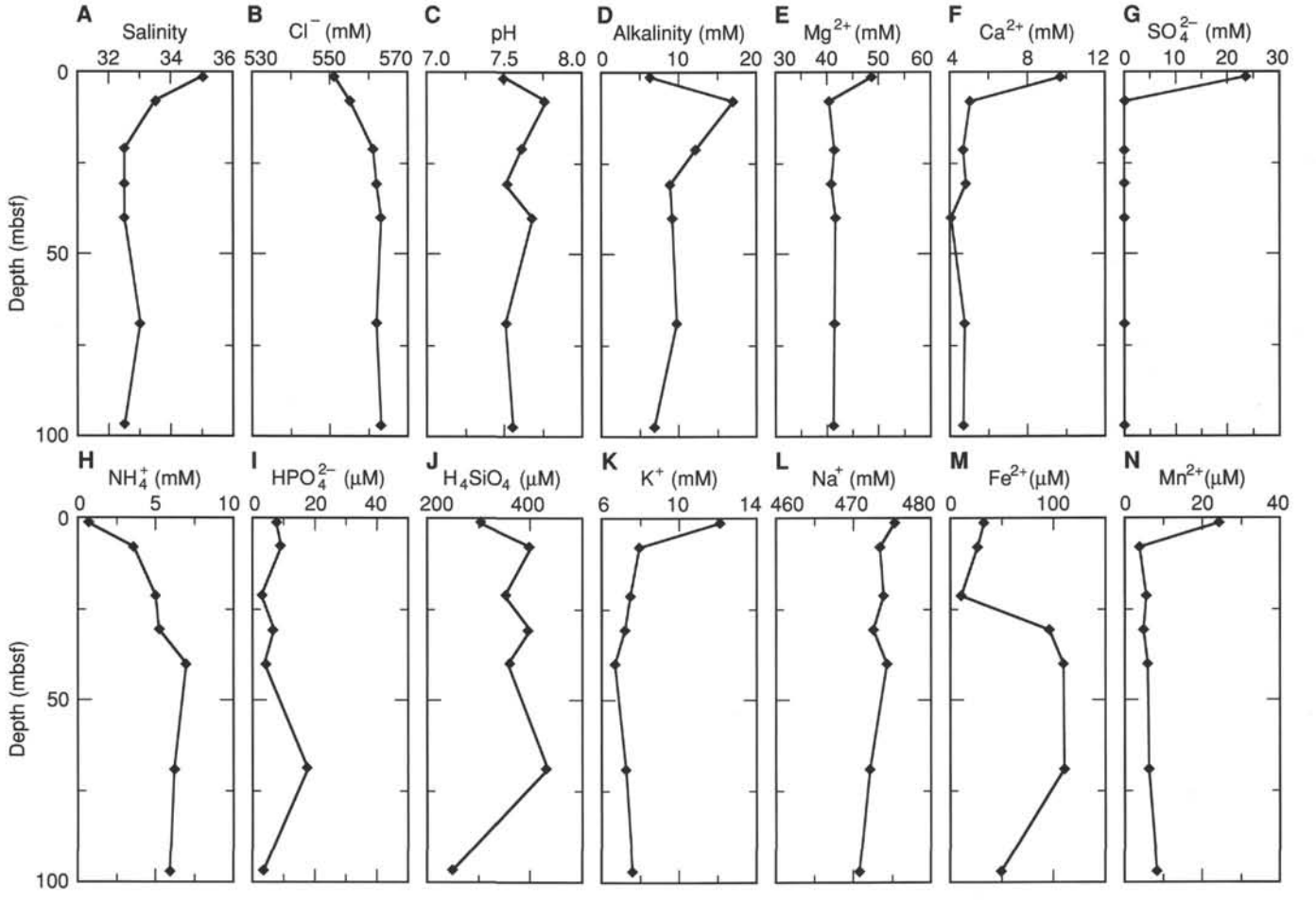

Figure 22. Downcore variation in pore-water chemistry: **A.** Salinity. **B.** Chloride. **C.** pH. **D.** Alkalinity. **E.** Magnesium. **F.** Calcium. **G.** Sulfate. **H.** Ammonium. **I.** Phosphate. **J.** Silica. **K.** Potassium. **L.** Sodium. **M.** Iron. **N.** Manganese.

Table 10. Major element composition (wt%) of sediment samples, Site 934.

Core, section, interval (cm)	Depth (mbsf)	Lithology	SiO_2	TiO_2	Al_2O_3	Fe_2O_3	MnO	MgO	CaO	Na_2O	K_2O	P_2O_5	Total	LOI
155-934A-														
2H-6, 40–45	12.20	Mud	66.00	1.01	18.89	6.85	0.11	1.80	0.94	1.47	2.68	0.15	99.90	6.98
8H-5, 111–115	67.17	Mud	62.05	1.01	21.83	7.83	0.11	2.04	0.80	1.20	2.92	0.20	100.00	8.27

Notes: Total iron is reported as Fe_2O_3. LOI = loss on ignition.

Table 11. Trace element composition (ppm) of sediment samples, Site 934.

Core, section, interval (cm)	Depth (mbsf)	Lithology	Ba	Ce	Cr	Cu	Nb	Ni	Rb	Sr	V	Y	Zn	Zr
155-934A-														
2H-6, 40–45	12.20	Mud	445	97	56	26	21	29	116	160	74	38	110	287
8H-5, 111–115	67.17	Mud	467	113	64	32	21	35	128	151	81	36	122	218

sities increase downhole from about 1.85 to 1.95 g/cm^3. This trend continues below the sand beds of Unit IV. Wet-bulk densities at the base of the hole are about 2.0 g/cm^3. The GRAPE data reflect the general trends in wet-bulk density but are characterized by densities that are 0.2 to 0.4 g/cm^3 lower than the discrete-sample values (Fig. 23).

Grain density values are virtually constant downhole, 2.7 to 2.8 g/cm^3 (Table 12). Values from sand- and silt-rich samples are only slightly lower than those determined from clay-rich samples.

Between 19 and 64 mbsf, the variation in water content and porosity may relate to fluctuations in the sedimentation rate or lithology. The abrupt increase in bulk density in Unit III suggests prior consolidation elsewhere or a period of negligible sedimentation rates.

Compressional-wave Velocity

Transverse velocities ranging from 1492 to 1510 m/s were measured by the PWL in Holes 934A and 934B for the upper 7.1 m. Longitudinal velocities ranging from 1483 to 1524 m/s were measured with the DSV in the upper 5.5 m of Hole 934A. Because core expansion produced pervasive microfractures in the sediment, neither of the techniques was capable of consistently transmitting an acoustic signal with sufficient strength through sediment from greater depths.

Shear Strength

Measurements of undrained shear strength were made using the motorized shear vane on most cores from Hole 934A cores (Table 13). Below 45 mbsf, compressive strengths were determined using a pocket penetrometer. There is good correlation between shear-strength values assumed from the compressive strength and those determined by the motorized shear vane.

The strength profile can be divided into four intervals. The upper two intervals, from the seafloor to 13 mbsf, and 19 to 43 mbsf, exhibit gradual increases with depth with differing gradients and low variability (Fig. 24). The third interval (44 to 64 mbsf) shows a decrease from about 50 to 25 kPa with increased variability. Below the sand beds of lithologic Unit IV, which is the deepest interval, shear strengths are widely scattered between 28 and 69 kPa, and the correlation between shear-vane and pocket-penetrometer results is poor. The increased variability in Units IV and V probably results from the higher sand content of this interval. The ratio of residual to peak shear strength decreases downhole (Fig. 24). This trend is expected for the downhole increases in shear strengths and coarse-grained sediment.

The change in the shear-strength profile at the boundary of Units II and III supports the interpretation of increased consolidation based on the change in wet-bulk density. As the consolidation of Unit III is only slightly greater than Unit II, it is suggested that if Unit III is a mass transport deposit, the sediment were deposited only a short period before slumping. The downhole decrease in shear strength within Unit III implies that less consolidated, possibly younger material was incorporated in this unit. This characteristic is in contrast with debris-flow material recovered in previous holes, which is well consolidated and shows significantly higher shear strength.

Resistivity

Longitudinal and transverse resistivity profiles show an overall increase downhole, divided into four intervals similar to those shown by the index properties and shear strength (Table 14, Fig. 25). From the seafloor to 13 mbsf, resistivity gradually increases from about 0.2 Ωm to 0.4 Ωm. The increase is reduced between 19 and 42 mbsf (0.38 to 0.48 Ωm). Below 42 mbsf, there is little overall increase in longitudinal resistivity.

Resistivity anisotropy varies widely in Units I through III (Fig. 25). The laminated and thin-bedded sediment of Unit II is characterized by a slight negative anisotropy. Anisotropy is more strongly negative in Unit III. In Units IV and V the sediment is more nearly isotropic.

DOWNHOLE LOGGING

Logging Operations and Quality of Logs

After drilling and coring were finished at Hole 934B, the drill pipe was raised to 77.9 mbsf, and preparations were made for raising the pipe to 48.9 mbsf during logging. Because of the short total depth drilled (108.2 mbsf), we used a shortened version of the Quad-combination tool string to maximize the logged interval. This shorter (10 m) tool string included the resistivity (DITE/SFL) and the natural gamma (NGT) tools.

The tool string would not enter the open hole; so, it was retrieved and the hole reamed by lowering the drill pipe to the bottom of the borehole. Sediment had filled the borehole, and we re-drilled to 108.2 mbsf. The tool string then passed into the open hole, and we logged (upgoing and downgoing) the interval between 48.2 and 105 mbsf. Between 0 and 48.2 mbsf, we obtained logs through the pipe, but only the attenuated gamma-ray logs may provide useful results after shore-based processing. The wireline heave compensator (WHC) was not used during this logging run, which may have produced small depth mismatches among different tools within the string and between the logs and the retrieved cores. The absence of a caliper during this logging run prevents us from making a detailed assessment of log quality, but data appear to be of good quality on the basis of good correlation with recovered cores.

Table 12. Index properties at Site 934.

Core, section, interval (cm)	Depth (mbsf)	Water content (%)	Wet-bulk density (g/cm^3)	Grain density (g/cm^3)	Dry-bulk density (g/cm^3)	Porosity (%)	Void ratio
155-934A-							
1H-1, 24–26	0.24	50.5	1.51	2.72	0.73	73.1	2.72
1H-1, 91–93	0.91	58.7	1.42	2.82	0.57	79.6	3.91
1H-2, 83–85	2.33	41.5	1.66	2.80	0.95	65.9	1.93
1H-3, 84–86	3.84	38.2	1.70	2.69	1.03	61.9	1.62
2H-1, 122–124	5.52	41.8	1.65	2.81	0.95	66.3	1.97
2H-2, 127–129	7.07	38.9	1.69	2.79	1.02	63.4	1.73
2H-3, 125–127	8.55	39.0	1.67	2.75	1.01	63.2	1.72
2H-4, 119–121	9.99	38.2	1.68	2.73	1.03	62.3	1.65
2H-5, 100–102	11.30	35.3	1.77	2.78	1.12	59.6	1.48
2H-6, 88–90	12.68	37.8	1.66	2.73	1.04	61.8	1.62
2H-7, 34–36	13.64	36.4	1.70	2.78	1.09	60.8	1.55
2H-7, 65–67	13.95	35.2	1.75	2.72	1.11	59.0	1.44
3H-1, 19–21	13.99	34.1	1.78	2.72	1.15	57.8	1.37
3H-2, 59–61	15.89	34.6	1.80	2.74	1.13	58.5	1.41
3H-3, 120–122	18.00	25.3	1.95	2.69	1.42	47.0	0.89
3H-4, 104–106	19.34	33.8	1.79	2.71	1.15	57.5	1.35
3H-5, 71–73	20.51	36.7	1.75	2.77	1.08	61.0	1.57
3H-6, 123–125	22.53	35.6	1.75	2.72	1.10	59.5	1.47
3H-7, 12–14	22.92	34.2	1.79	2.77	1.15	58.4	1.40
4H-1, 50–52	23.80	32.1	1.81	2.72	1.21	55.6	1.25
4H-2, 59–61	25.39	31.3	1.85	2.79	1.25	55.4	1.24
4H-3, 124–126	27.54	32.4	1.82	2.76	1.21	56.4	1.29
4H-4, 112–114	28.92	33.7	1.81	2.78	1.17	57.9	1.38
4H-5, 83–85	30.13	35.1	1.77	2.74	1.12	59.1	1.45
4H-6, 90–92	31.70	31.5	1.82	2.70	1.22	54.8	1.21
4H-7, 45–47	32.75	31.9	1.84	2.77	1.22	55.8	1.26
5H-1, 41–43	33.21	31.8	1.83	2.74	1.22	55.4	1.24
5H-2, 85–87	35.15	33.1	1.80	2.72	1.18	56.7	1.31
5H-3, 88–90	36.68	34.8	1.78	2.71	1.12	58.5	1.41
5H-4, 17–19	37.47	34.6	1.79	2.72	1.13	58.5	1.41
5H-4, 96–98	38.26	36.4	1.75	2.71	1.08	60.2	1.51
5H-5, 82–84	39.62	35.6	1.81	2.80	1.12	60.1	1.51
5H-6, 83–85	41.13	35.6	1.78	2.72	1.10	59.5	1.47
5H-7, 24–26	42.04	34.7	1.78	2.76	1.13	58.8	1.43
6H-1, 76–78	43.06	32.9	1.71	2.73	1.19	56.6	1.31
6H-2, 60–62	44.40	31.8	1.83	2.72	1.22	55.4	1.24
6H-3, 33–35	45.63	29.8	1.89	2.79	1.29	53.7	1.16
6H-5, 6–8	47.53	28.8	1.93	2.80	1.33	52.5	1.11
6H-6, 69–71	49.66	29.8	1.87	2.75	1.29	53.3	1.14
6H-7, 105–107	51.52	30.3	1.87	2.76	1.27	54.0	1.17
7H-1, 48–50	52.28	26.4	1.94	2.74	1.40	49.0	0.96
7H-2, 98–100	54.28	29.8	1.87	2.80	1.30	53.7	1.16
7H-3, 60–62	55.40	28.6	1.89	2.71	1.32	51.5	1.06
7H-4, 98–100	57.28	27.9	1.92	2.72	1.34	50.7	1.03
7H-5, 97–99	58.77	27.7	1.92	2.72	1.35	50.4	1.02
7H-6, 62–64	59.92	28.9	1.91	2.73	1.31	52.0	1.08
7H-7, 66–68	61.46	30.5	1.85	2.70	1.25	53.6	1.16
8H-2, 39–41	62.06	29.0	1.92	2.76	1.32	52.4	1.10
8H-3, 91–93	64.04	25.8	1.95	2.68	1.41	47.6	0.91
8H-7, 75–77	69.81	26.6	1.95	2.76	1.40	49.4	0.98
9H-2, 55–57	72.85	29.3	1.87	2.70	1.29	52.2	1.09
9H-5, 18–20	75.94	14.5	2.29	2.74	1.88	31.2	0.45
10H-2, 102–104	82.82	30.1	1.90	2.82	1.29	54.2	1.18
10H-3, 80–82	84.10	27.4	1.92	2.72	1.36	50.0	1.00
10H-4, 37–39	85.17	31.1	1.84	2.69	1.23	54.2	1.18
10H-5, 115–117	87.45	15.5	2.19	2.66	1.80	32.3	0.48
10H-6, 20–22	88.00	29.3	1.91	2.71	1.29	52.3	1.10
10H-7, 75–77	90.05	27.0	1.95	2.79	1.39	50.2	1.01
11H-1, 81–83	90.61	30.5	1.88	2.71	1.25	53.7	1.16
11H-2, 64–66	91.94	27.7	1.92	2.67	1.34	50.0	1.00
11H-3, 30–32	93.10	23.3	1.99	2.68	1.49	44.3	0.80
11H-4, 74–76	95.04	27.6	1.96	2.80	1.37	50.9	1.04
11H-5, 35–37	96.15	28.6	1.93	2.78	1.33	52.1	1.09
11H-6, 35–37	97.65	26.9	1.94	2.72	1.38	49.4	0.98
11H-7, 6–8	98.86	23.8	2.04	2.79	1.51	46.0	0.85
12H-1, 43–45	99.73	29.7	1.90	2.81	1.30	53.7	1.16
12H-2, 34–36	101.14	27.1	1.94	2.73	1.37	49.8	0.99
12H-3, 87–89	103.17	27.5	1.93	2.71	1.35	50.1	1.00
12H-4, 32–34	104.12	27.4	1.95	2.77	1.37	50.5	1.02
12H-4, 75–77	104.55	25.6	1.98	2.72	1.42	47.7	0.91
12H-5, 24–26	105.54	23.5	1.96	2.73	1.50	45.1	0.82
12H-6, 44–46	107.24	25.7	1.96	2.75	1.42	48.2	0.93
12H-7, 28–30	108.58	24.8	2.00	2.73	1.45	46.9	0.88

Results

The gamma-ray (and some of the key resistivity) data from the upgoing logging run are shown in Figure 26. Low gamma-ray values correlate with low resistivity intervals. The gamma-ray response appears to be primarily controlled by variations in the amount of thorium and potassium, while the amount of uranium remains approximately constant at about 2 ppm. The interval between 73 and 78 mbsf indicates slight enrichment in uranium (3 ppm) with respect to the rest of the logged interval (average of 2 ppm). Two intervals of low overall gamma-ray response were observed between 71 and 73 mbsf and between 78 to 85 mbsf. Electrical resistivity data show three intervals of distinctly lower values: at 71 to 73, 77 to 79, and 87 to 94 mbsf. From 95 to 105 mbsf, resistivity data show a downhole decrease, suggesting an overall decrease in porosity downhole.

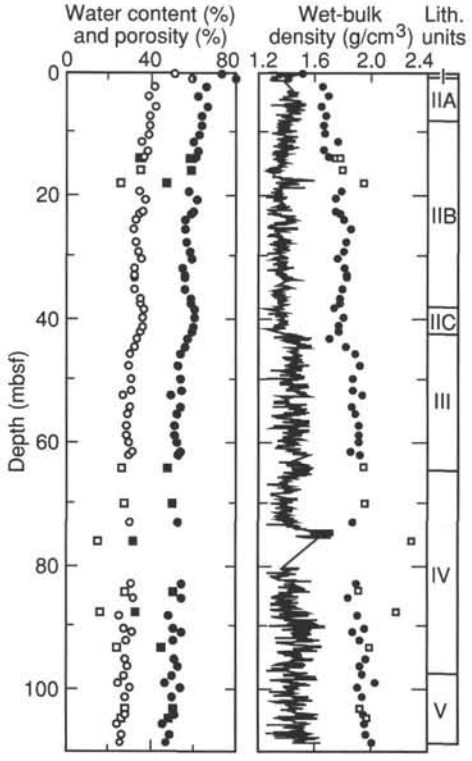

Figure 23. Water content (open symbols), porosity (solid symbols), and wet-bulk density as determined for discrete samples and GRAPE (line) in Hole 934A. Circles = silty clay; squares = sand and sandy silt.

Correlation with Lithology

At this site, we attempted a preliminary correlation with lithostratigraphic observations. Lithologic units appear to be 1.5 m deeper in Hole 934B than those in Hole 934A, and logging measurements in Hole 934B appear to be 1 m deeper than the core measurements (Fig. 27). This discrepancy is within the expected accuracy of the measurements, but may have been exacerbated by our not using the WHC.

Comparison of the lithologic observations with the resistivity and gamma-ray data shows that silty clay intervals correlate well with low resistivity sections and with intermediate to low gamma-ray response. The intervals having silty-clay and clay clasts indicate a marked increase in resistivity and an increase in gamma-ray response, probably the result of the presence of clay clasts. The lowest gamma readings, observed between 78 and 85 mbsf, correspond to a sand-rich unit, although, locally, clay clasts affect both gamma-ray and resistivity values. High-resolution resistivity data (IDVR, Fig. 26) indicate three large peaks in resistivity, interpreted to be caused by the abundant organic material observed in some turbidite beds. The lower portion of the logged interval (94–102 mbsf) shows a downhole decrease in resistivity, similar to that observed between 78 and 85 mbsf. This suggests that the sand-rich unit identified as the base of lithostratigraphic Unit IV may be thicker, extending to at least 102 mbsf in Hole 934B (Figs. 4 and 27). This decrease in resistivity also suggests that the number of clay clasts may decrease downhole within the bed.

IN-SITU TEMPERATURE MEASUREMENTS

Temperature gradients and heat flow were determined using two downhole measurements and the bottom-water (mud-line) temperature. Two ADARA measurement were made during Cores 934A-4H (32.8 mbsf) and -9H (70.8 mbsf) using instrument number 12. The mud-line temperature of 2.4°C measured from this instrument was used as the reference bottom-seawater temperature at Site 934. Successful measurements resulted in extrapolated equilibrium temperatures of 3.76°C at 32.8 mbsf, and 4.85°C at 70.8 mbsf.

Equilibrium temperatures, extrapolated from synthetic curves constructed to fit transient temperature data, are plotted as a function of depth (mbsf) in Figure 28. Using the ADARA mud-line temperature, and the sub-bottom temperatures from the two ADARA measurements downhole, the geothermal temperature gradient can be approximated by a linear mean of 34.45°C/km. We calculated heat flow by adopting the constant geothermal temperature gradient of 34.45°C/km and a linear increase in thermal conductivity, K, of 1.1 ±

Table 13. Undrained shear strength at Site 934.

Core, section, interval (cm)	Depth (mbsf)	Peak undrained shear strength (kPa)	Residual undrained shear strength (kPa)	Unconfined compressive strength* (kPa)
155-934A-				
1H-1, 25	0.25	6.8	5.2	
1H-1, 92	0.92	4.0	2.9	
1H-2, 92	2.42	6.2	4.5	
1H-3, 85	3.85	7.6	5.2	
2H-1, 125	5.55	8.0	5.4	
2H-2, 128	7.08	8.8	6.5	
2H-3, 126	8.56	8.2	6.0	
2H-4, 120	10.00	8.0	6.1	
2H-5, 101	11.31	10.2	7.4	
2H-6, 89	12.69	12.0	8.1	
2H-7, 35	13.65	9.9	6.7	
3H-4, 105	19.35	12.0	8.0	
3H-5, 72	20.52	16.5	10.5	
3H-6, 124	22.54	16.4	10.7	
3H-7, 13	22.93	13.9	9.5	
4H-1, 51	23.81	21.1	13.4	
4H-2, 60	25.40	20.0	12.1	
4H-3, 125	27.55	19.5	13.2	
4H-4, 113	28.93	16.7	10.6	
4H-5, 84	30.14	18.1	11.6	
4H-6, 91	31.71	22.7	14.2	
4H-7, 46	32.76	20.6	13.0	
5H-1, 42	33.22	27.4	16.2	
5H-2, 86	35.16	26.6	16.1	
5H-3, 89	36.69	27.7	14.7	
5H-4, 18	37.48	26.9	13.8	
5H-4, 97	38.27	28.7	15.4	
5H-5, 83	39.63	34.0	13.7	
5H-6, 84	41.14	28.8	16.6	
5H-7, 25	42.05	26.9	13.5	
6H-1, 77	43.07	28.3	17.3	
6H-2, 61	44.41	39.9	21.2	
6H-3, 34	45.64	59.1	28.3	98.1
6H-5, 7	47.54	33.7	19.5	73.6
6H-6, 70	49.67	41.0	20.0	83.4
6H-7, 106	51.53	32.2	15.3	78.5
7H-1, 49	52.29	25.2	11.6	63.8
7H-2, 99	54.29	24.9	12.8	49.1
7H-3, 61	55.41	26.6	12.9	58.9
7H-4, 99	57.29	32.0	19.0	54.0
7H-5, 98	58.78	34.5	19.7	54.0
7H-6, 63	59.93	28.6	16.8	58.9
7H-7, 67	61.47	26.0	16.3	34.3
8H-2, 40	62.07	42.7	18.0	88.3
8H-3, 92	64.05	31.7	14.0	83.4
10H-2, 103	82.83			166.8
10H-6, 76	88.56			186.4
11H-1, 82	90.62			147.2
11H-2, 65	91.95			122.6
11H-4, 76	95.06	47.3		161.9
11H-5, 36	96.16			112.8
11H-6, 36	97.66	39.6		117.7
11H-7, 7	98.87	69.4		225.6
12H-1, 7	99.37	27.8		
12H-1, 41	99.71			73.6
12H-2, 36	101.16			122.6
12H-4, 33	104.10	45.8		
12H-5, 25	105.60	46.3		
12H-6, 46	107.30	44.7		186.4
12H-7, 28	108.58			181.5
12H-7, 46	108.80	59.1		

Note: *Unconfined compressive strength (q_u) can be used to approximate undrained shear strength (S_u) by the relationship $q_u = 2S_u$.

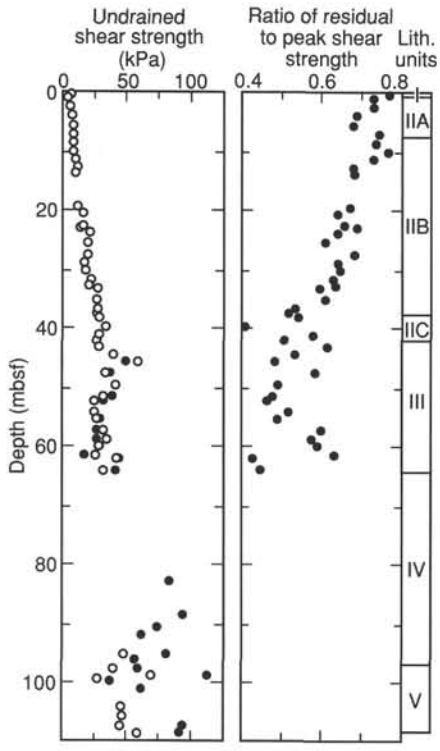

Figure 24. Left: undrained shear strength (open circles) and assumed undrained shear strength derived from unconfined compressive strength (closed circles); right: ratio of residual to peak undrained shear strength in Hole 934A.

0.15 W/(m·K), which is an average of regression estimates at 80 mbsf. This results in a calculated heat flow of 37.95 mW/m^2.

SYNTHESIS AND SIGNIFICANCE

Stratigraphic Synthesis

Surficial Foraminifer-Nannofossil Clay (Unit I)

As at previous sites, a Holocene calcareous clay containing foraminifers and nannofossils is found at the mud line (Fig. 29). The unit is 0.87 m thick, with a brown diagenetic crust at 0.48 mbsf.

Overbank Sediment of the Abandoned Meander Loop (Unit II)

Unit II (0.87–42.30 mbsf) consists of mud with thin beds and laminae of silt and sand. The unit is interpreted as sediment that filled the abandoned meander bend by spillover from turbidity currents flowing down the main Amazon Channel after the meander was cut off. The lower part of the unit shows a coarsening-upward trend, the upper part a fining-upward trend. Subunit IIA (0.87–7.70 mbsf) consists of prominently color-banded clays, some of which are mud turbidites with hemipelagic tops containing nannofossils. Subunit IIB (7.70–37.89 mbsf) consists of silty clays with silt laminae and some graded beds of silty sand, a few of which are more than 1 m thick. Subunit IIC (37.89–42.30 mbsf) consists of mud that is faintly color banded and mottled. Total organic-carbon concentrations in mud samples range from 0.8% to 1.1%. Total sulfur is as much as 0.16% in the upper part of the sediment column, but below 29 mbsf no sulfur was detected.

Muddy Mass Flow (Unit III)

Unit III (42.30–64.56 mbsf) consists of mud with laminae and beds of silt and sand that have undergone wet-sediment deformation, including plastic folding, injection of sand and mud, and partial mixing of different sediment types. The unit is interpreted as a mass-flow deposit ("slump") formed by sediment failure on the adjacent channel wall. This unit has a markedly higher wet-bulk density and shear strength compared with Unit II. Shear strength within the unit decreases downhole, suggesting either stratigraphic inversion or poor drainage from the lower part of the mass flow.

Channel Fill Sand (Unit IV)

Unit IV (64.56–97.03 mbsf) consists of medium to very thick beds of very fine- to medium-grained sand and coarse silt, with thin interbedded mud beds. Many of the sand beds contain mud clasts. At the top of the unit, an 18-m-thick sand bed contains folded mud clasts up to 70 cm thick. Near the base of the bed, patches of 1- to 2-mm

Table 14. Electrical resistivity at Site 934.

Core, section, interval (cm)	Depth (mbsf)	Longitudinal resistivity (Ωm)	Transverse resistivity (Ωm)
155-934A-			
1H-1, 25	0.25	0.224	0.224
1H-1, 92	0.92	0.189	0.221
1H-2, 85	2.35	0.228	0.227
1H-3, 85	3.85	0.262	0.255
2H-1, 123	5.53	0.307	0.284
2H-2, 128	7.08	0.331	0.329
2H-3, 126	8.56	0.312	0.349
2H-4, 120	10.00	0.353	0.370
2H-5, 101	11.31	0.412	0.338
2H-6, 89	12.69	0.338	0.371
2H-7, 35	13.65	0.392	0.350
3H-4, 105	19.35	0.378	0.392
3H-5, 72	20.52	0.435	0.417
3H-6, 124	22.54	0.413	0.390
3H-7, 13	22.93	0.385	0.420
4H-1, 51	23.81	0.453	0.376
4H-2, 60	25.40	0.383	0.393
4H-3, 125	27.55	0.511	0.443
4H-4, 113	28.93	0.432	0.395
4H-5, 84	30.14	0.414	0.432
4H-6, 91	31.71	0.473	0.424
4H-7, 46	32.76	0.456	0.445
5H-1, 42	33.22	0.513	0.461
5H-2, 86	35.16	0.439	0.439
5H-3, 89	36.69	0.443	0.478
5H-4, 18	37.48	0.531	0.434
5H-4, 97	38.27	0.423	0.404
5H-5, 83	39.63	0.406	0.426
5H-6, 84	41.14	0.432	0.407
5H-7, 25	42.05	0.477	0.437
6H-1, 82	43.12	0.536	0.501
6H-2, 61	44.41	0.638	0.480
6H-3, 34	45.64	0.466	0.383
6H-5, 7	47.54	0.525	0.410
6H-6, 70	49.67	0.438	0.392
6H-7, 106	51.53	0.664	0.562
7H-1, 49	52.29	0.466	0.430
7H-2, 99	54.29	0.455	0.405
7H-3, 61	55.41	0.552	0.448
7H-4, 99	57.29	0.449	0.421
7H-5, 98	58.78	0.464	0.437
7H-6, 63	59.93	0.465	0.434
7H-7, 67	61.47	0.447	0.451
8H-2, 40	62.07	0.442	0.478
8H-3, 92	64.05	0.477	0.453
9H-2, 55	72.85	0.407	0.382
10H-2, 103	82.83	0.488	0.470
10H-3, 80	84.10	0.403	0.394
10H-4, 38	85.18	0.409	0.391
10H-5, 20	86.50	0.384	0.403
10H-6, 76	88.56	0.420	0.435
11H-1, 82	90.62	0.424	0.412
11H-2, 65	91.95	0.461	0.436
11H-4, 76	95.06	0.443	0.452
11H-5, 36	96.16	0.413	0.411
11H-6, 36	97.66	0.480	0.435
11H-7, 7	98.87	0.474	0.473
12H-1, 44	99.74	0.417	0.411
12H-2, 36	101.16	0.423	0.444
12H-3, 88	103.18	0.448	0.435
12H-4, 33	104.13	0.426	0.427
12H-5, 25	105.55	0.460	0.441
12H-6, 46	107.26	0.478	0.457
12H-7, 30	108.60	0.470	0.483

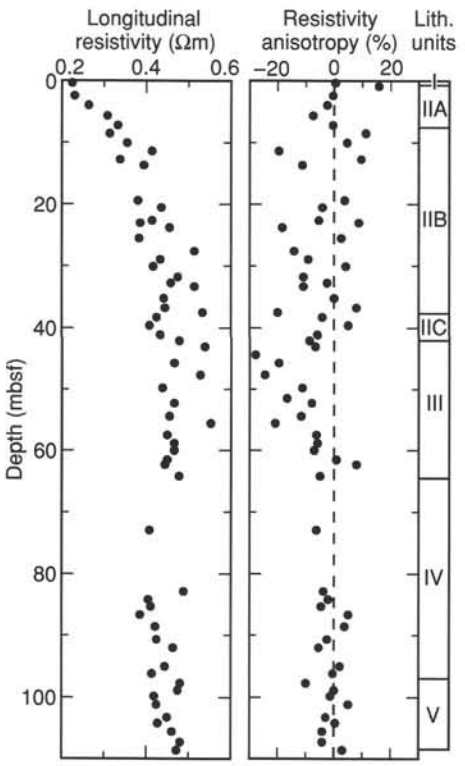

Figure 25. Longitudinal resistivity and resistivity anisotropy in Hole 934A.

quartzose sand, some granules, shell debris, and plant fragments are found. This unit is interpreted as the original channel floor sediment before meander abandonment. Beds thicken from Hole 934A to Hole 934B, which is 50 m to the south and closer to the original channel axis. Mud clasts show shear strengths of 50–120 kPa, compared with 25–50 kPa in Unit III.

Pre-channel Silt and Mud (Unit V)

Unit V (97.03–108.8 mbsf) consists of mud with thin beds and laminae of silt and sand. The sediment contains few planktonic and upper bathyal benthic foraminifers. Shear strength is similar to that of the mud clasts in Unit IV, whereas wet-bulk density is a little higher (2.0 g/cm^3 in Unit V, 1.9 g/cm^3 in Unit IV). This unit is interpreted as levee sediment predating the formation of the channel in the meander loop.

Implications

Holes at Site 934 penetrated channel-floor sediment preserved in a cutoff meander bend of the main (Amazon) channel that is overlain by sediment that accumulated after the meander loop was abandoned. The consequent decrease in sinuosity would have caused about 15 m of incision of the straighter main channel (Pirmez, 1994). The present seafloor in the abandoned bend lies 55 m above the main channel floor, so the channel floor before incision would have aggraded to 40 mbsf. The base of the Amazon Channel-levee System occurs at 160 mbsf.

Foraminifer and calcareous nannofossil abundances are generally very low except in Unit I. A detailed abundance profile in Unit I showed that *G. fibriata* is absent below 0.3 mbsf, *G. menardii* below 0.4 mbsf, and *G. tumida* below 0.9 mbsf. The *G. tumida* marker has been dated at about 9 ka (G. Jones, pers. comm., 1994). This means that the extreme top of Subunit IIA is of earliest Holocene age (9–10 ka). Otherwise, the paucity of microfossils precludes identification of stratigraphic markers at the site. Variation in magnetic inclination with a wavelength of about 20 m in Unit II is interpreted as secular variation, and implies a sedimentation rate of the order of 14 m/k.y. This rate is consistent with the overall thickness of the Amazon Channel-levee System at this site.

We interpret the sediment at this site to represent pre-channel silt and mud (Unit V), channel fill sand (Unit IV), a muddy mass flow (Unit III), and subsequent overbank sedimentation into the abandoned meander loop (Unit II). This is capped by Holocene hemipelagic calcareous clay (Unit I). The 18-m-thick sand bed at the top of Unit IV was deposited by a large flow or set of flows, capable of transporting granules of quartz and meter-size boulders of mud. The bed may have been emplaced as a sandy debris flow (e.g., Postma, 1986). By coring and logging Unit IV, we have for the first time documented the character of the sandy fill of an active aggrading channel in a modern deep-sea fan, where transport distance and morphology of channel and levee are known. This will provide an important reference for the interpretation of channel processes and of ancient channel-fill deposits. The log data are strongly influenced by the presence of clay clasts in the channel-fill sediment. Without the core, we would have interpreted the gamma-ray and resistivity logs to indicate thinner sand beds, separated by interbedded muds. The logs thus provide a possibly misleading impression of the size of sand depositional units and the potential vertical connectivity of sand bodies.

The top of Unit IV, the channel-fill sequence, is at 65–70 mbsf (the range is because of the uncertainty in the depths of the two holes and the logs). The top of Unit III, the mass flow, is at 45 mbsf. This compares with an estimated level of 40 mbsf for the channel floor immediately before cutoff. These data suggest that the mass flow in Unit III forms part of the aggraded channel-fill in the cutoff and may have been responsible for partially blocking the meander loop, triggering the cutoff.

The sand types recovered from Site 934 have similar composition and texture to sand types from the nearby Guiana Basin (Damuth and Fairbridge, 1970), except that samples from Site 934 appear to contain less feldspar. Medium to coarse sand grains are texturally distinct from the fine sand and consist of about 90% well-rounded monocrystalline quartz, many with iron-rich surface coatings. Fragments of microlitic volcanic rocks, clinopyroxene, hypersthene, and rare olivine indicate a contribution from mafic igneous rocks. The olivine is particularly labile and could not have survived even moderate chemical weathering.

REFERENCES*

Bouma, A.H., 1962. *Sedimentology of Some Flysch Deposits: A Graphic Approach to Facies Interpretation:* Amsterdam (Elsevier).

Damuth, J.E., 1977. Late Quaternary sedimentation in the western equatorial Atlantic. *Geol. Soc. Am. Bull.*, 88:695–710.

Damuth, J.E., and Fairbridge, R.W., 1970. Equatorial Atlantic deep-sea arkosic sands and ice-age aridity in tropical South America. *Geol. Soc. Am. Bull.*, 81:189–206.

Flood, R.D., 1987. Side echoes from a sinuous fan channel obscure the structure of submarine fan channel/levee systems, Amazon fan. *Geo-Mar. Lett.*, 7:15–22.

Lowe, D.R., 1982. Sediment gravity flows: II. Depositional models with special reference to the deposits of high-density turbidity currents. *J. Sediment. Petrol.*, 52:279–297.

*Abbreviations for names of organizations and publications in ODP reference lists follow the style given in *Chemical Abstracts Service Source Index* (published by American Chemical Society).

Normark, W.R., Piper, D.J.W., and Hess, G.R., 1979. Distributary channels, sand lobes, and mesotopography of Navy submarine fan, California Borderland, with applications to ancient fan sediments. *Sedimentology*, 26:749–774.

Pirmez, C., 1994. Growth of a submarine meandering channel-levee system on the Amazon Fan [Ph.D. thesis]. Columbia Univ., New York.

Postma, G., 1986. Classification for sediment gravity-flow deposits based on flow conditions during sedimentation. *Geology*, 14:291–294.

Ms 155IR-110

NOTE: For all sites drilled, core-description forms ("barrel sheets") and core photographs can be found in Section 4, beginning on page 703. Forms containing smear-slide data can be found in Section 5, beginning on page 1199. GRAPE, index property, magnetic susceptibility, and natural gamma data are presented on CD-ROM (back pocket).

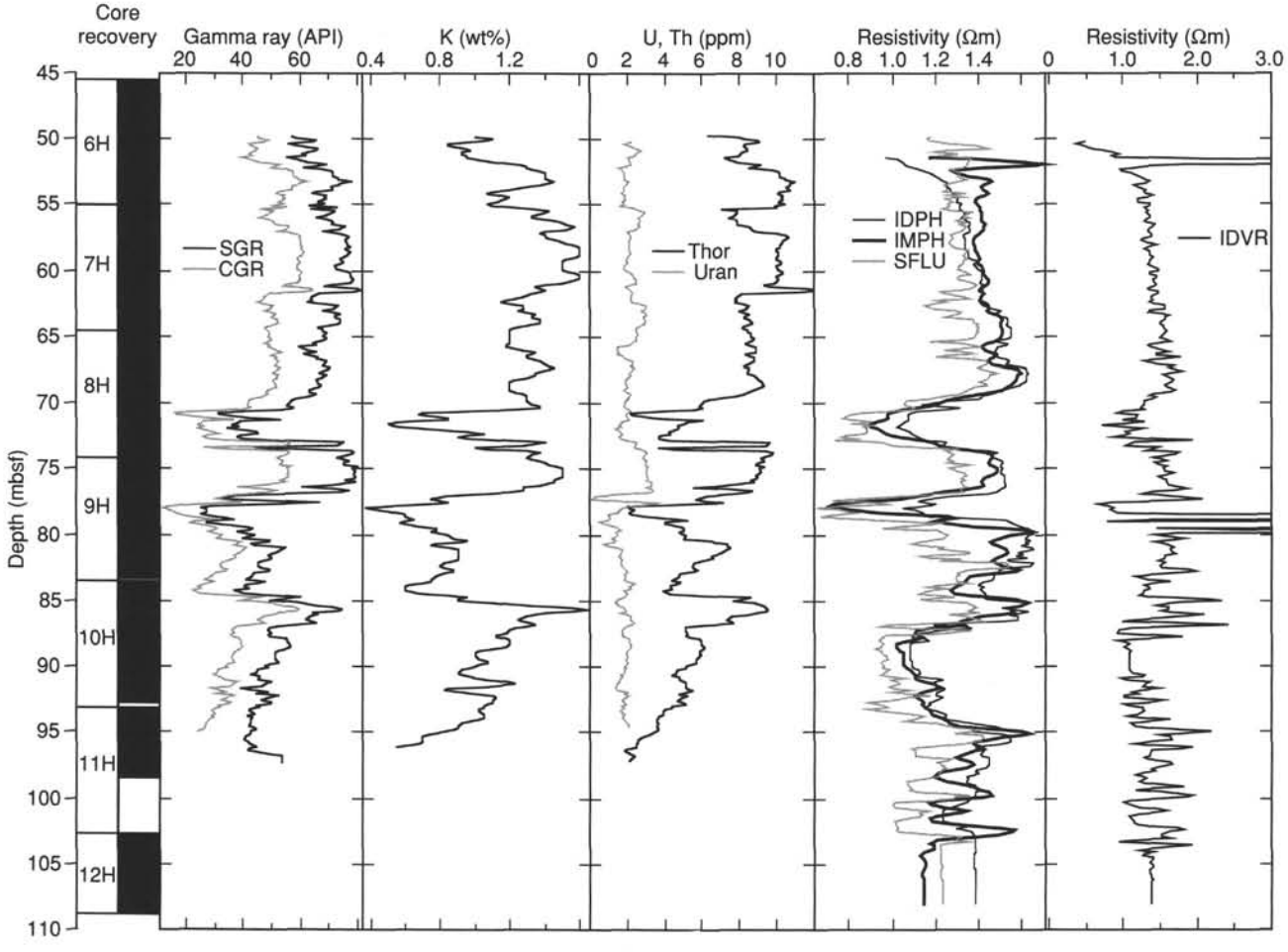

Figure 26. Logging data obtained with the NGT and DITE/SFL tools in Hole 934B. These are, left to right: SGR–spectroscopy gamma ray; CGR–uranium-free, computed gamma ray (Th + K); concentrations of potassium, uranium, and thorium; electrical resistivity, including the deep (IDPH) and medium (IMPH) phasor induction, shallow spherically focused (SFLU), and enhanced-resolution deep-phasor induction (IDVR).

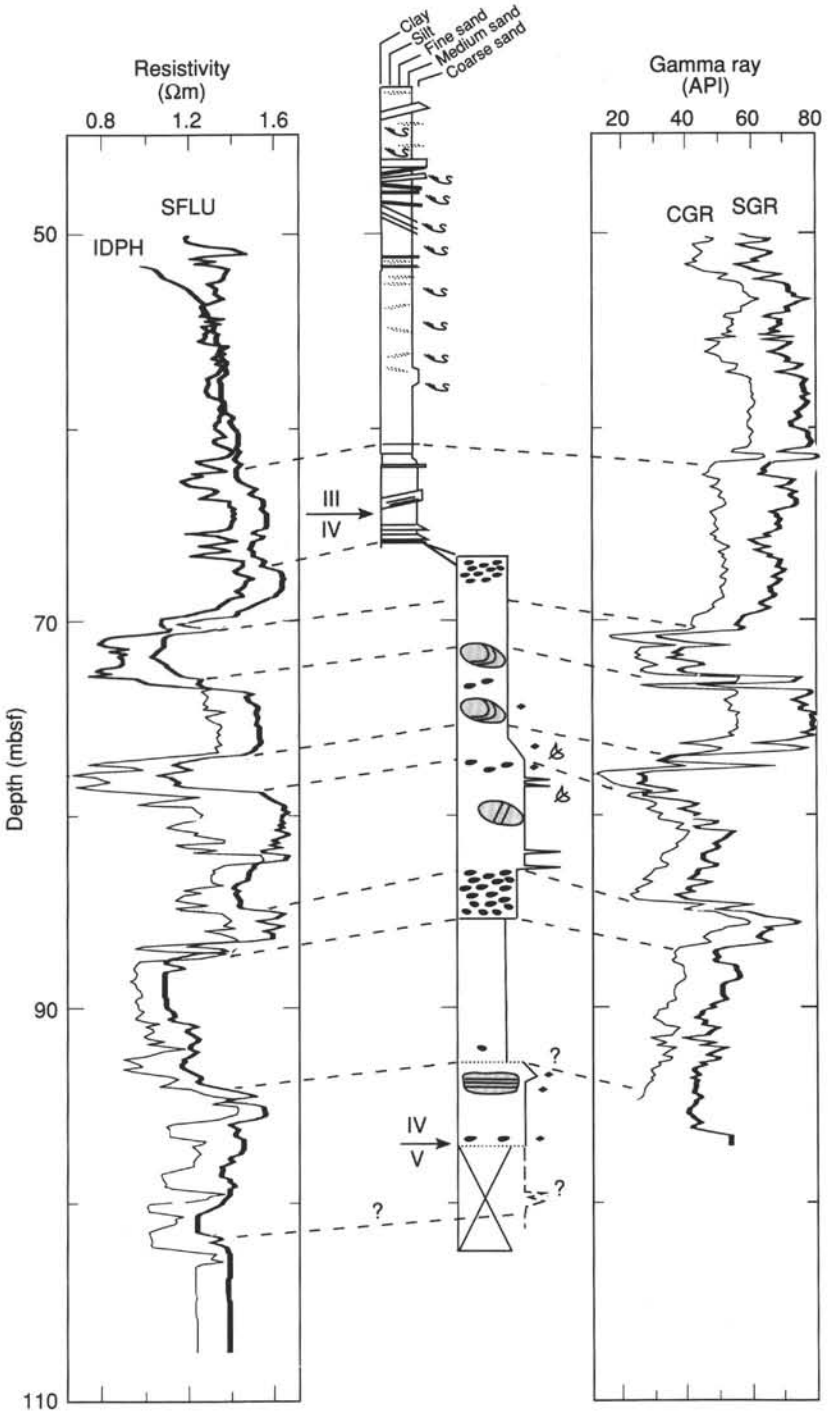

Figure 27. Comparison of logging to core observations in Hole 934B. Correlations of major bed boundaries and logging characteristics are marked by dashed lines. Units in Hole 934B are 1.5 m deeper in respect to Hole 934A; the core observations from Hole 934A are used above 73 mbsf. Logging data below 75 mbsf indicate an additional depth offset of 1 m in respect to the core observations at Hole 934B.

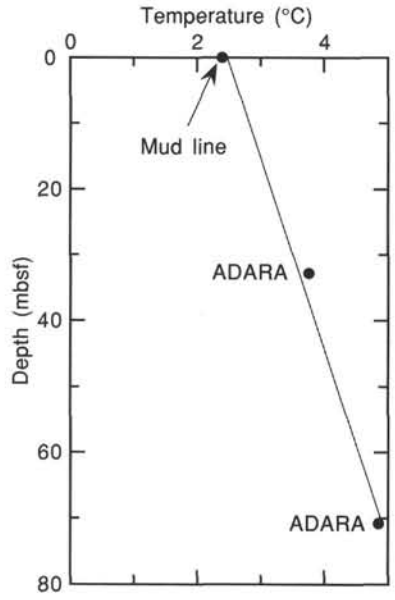

Figure 28. Estimated equilibrium temperatures in Hole 934A. A linear curve fit through the data suggests that reliable equilibrium temperatures were acquired that indicate a geothermal gradient of 34.45°C/km.

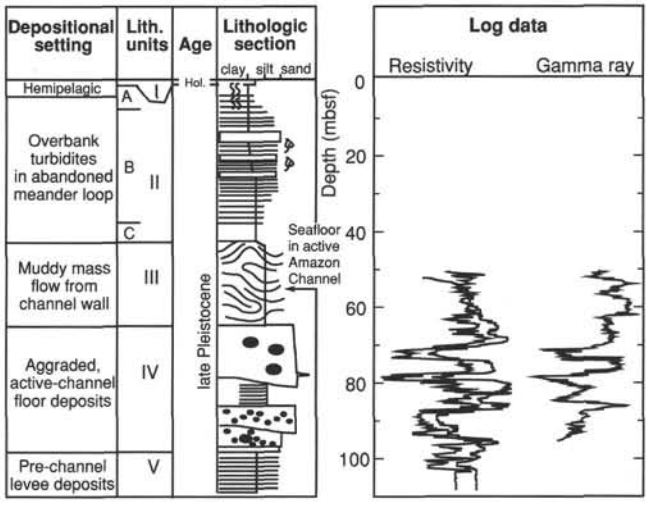

Figure. 29. Summary of lithostratigraphy, showing gamma-ray and resistivity logs.

SHORE-BASED LOG PROCESSING

HOLE 934B

Bottom felt: 3432 mbrf
Total penetration: 108.8 mbsf
Total core recovered: 106.9 m (98.3%)

Logging Runs

Logging string 1: DIT/NGT
Wireline heave compensator was used to counter ship heave.

Bottom-hole Assembly

The following bottom-hole assembly depths are as they appear on the logs after differential depth shift (see **Depth shift** section below) and depth shift to the seafloor. As such, there might be a discrepancy with the original depths given by the drillers on board. Possible reasons for depth discrepancies are ship heave, use of wireline heave compensator, and drill string and/or wireline stretch.

DIT/NGT: Bottom-hole assembly at 49 mbsf.

Processing

Depth shift: No differential depth shift necessary, as only one tool string was run.

All original logs have been depth shifted with reference to the seafloor (3433 mbrf). The amount used to depth shift the data to the seafloor corresponds to the seafloor depth observed on the logs (NGT), which differs one meter from the "bottom felt" depth given by the drillers. A list of the amount of differential depth shifts applied at this hole is available upon request.

Gamma-ray processing: NGT data have been processed to correct for borehole size and type of drilling fluid.

Quality Control

As no caliper was recorded, no quality control is possible at this hole. A constant value of 10.25 in. (which should theoretically correspond to a hole drilled with a 9.875-in. bit size) has been used in the NGT processing. Based on experience at other holes from Leg 155 this value is likely to be an underestimate of the actual borehole size; this would cause the NGT correction for borehole size to be underestimated as well.

Data recorded through pipe, such as the NGT data recorded above 49 mbsf, should be used only qualitatively because of the attenuation on the incoming signal.

Note: Details of standard shore-based processing procedures are found in the "Explanatory Notes" chapter, this volume. For further information about the logs, please contact:

Cristina Broglia
Phone: 914-365-8343
Fax: 914-365-3182
Email: chris@ldeo.columbia.edu

Elizabeth Pratson
Phone: 914-365-8313
Fax: 914-365-3182
Email: beth@ldeo.columbia.edu

935A Natural Gamma Ray-Resistivity-Velocity Logging Data (cont.)